A free boundary mechanobiological model of epithelial tissues

by

Tamara Tambyah
Bachelor of Mathematics, Bachelor of Science, 2018

School of Mathematical Sciences
Faculty of Science and Engineering
Queensland University of Technology

Supervised by
Prof Matthew Simpson and Dr Pascal Buenzli

A dissertation submitted in fulfilment
of the requirements for the degree of
Master of Philosophy

2020

Keywords: Moving boundary problem, Intracellular signalling, Cell–based model, Continuum model, Reaction–diffusion equations, Non-uniform growth.

In accordance with the requirements of the degree of Master of Philosophy in the School of Mathematical Sciences, I present the following thesis entitled,

A free boundary mechanobiological model of epithelial tissues

This work was performed under the supervision of Prof Matthew Simpson and Dr Pascal Buenzli. I declare that the work submitted in this thesis is my own, except as acknowledged in the text, and has not been previously submitted for the award of any other degree or diploma at Queensland University of Technology or any other institution.

Signed,

Tamara Tambyah
July 30, 2020

Acknowledgements

First and foremost, I would like to thank my supervisors, Prof Matthew Simpson and Dr Pascal Buenzli. I am grateful for your academic guidance and support throughout this degree.

I would also like to acknowledge and thank Mr Ryan Murphy. I appreciate your advice regarding computational and theoretical aspects of this work.

I acknowledge and thank the financial support of the Australian Research Council, and additionally funding provided by the School of Mathematical Sciences and ANZIAM. I am thankful for the opportunity to present my work at ANZIAM 2020.

Finally, I would like to extend my deepest gratitude to Mum and Sandy. Without your emotional support, advice and encouragement, I would never have made it this far. Thank you, this is for you.

Abstract

In this thesis, we couple intracellular signalling and cell–based mechanical properties to develop a novel free boundary mechanobiological model of epithelial tissue dynamics. Mechanobiological coupling is introduced at the cell level in a discrete modelling framework, and new reaction–diffusion equations are derived to describe tissue–level outcomes. The free boundary evolves as a result of the underlying biological mechanisms included in the discrete model. To demonstrate the accuracy of the continuum model, we compare numerical solutions of the discrete and continuum models for two different signalling pathways. First, we study the Rac–Rho pathway where cell– and tissue–level mechanics are directly related to intracellular signalling. Second, we study an activator–inhibitor system which gives rise to spatial and temporal patterning related to Turing patterns. In all cases, the continuum model and free boundary condition accurately reflect the cell–level processes included in the discrete model.

Contents

Chapter 1

Introduction

1.1 Overview

1.1.1 Context

A key research area in mathematical biology is studying cell migration [1, 2]. As tumours and wounds consist of a large number of cells, tumour development and wound healing is often studied as collective cell migration [3–6]. At the microscopic level, individual cells usually move in a random and irregular manner [1, 2]. This can result in collective cell migration which mimics cells migrating to heal an open wound, or to spread tumours [4, 7]. At the macroscopic level, collective cell migration is commonly modelled as a diffusion process [1, 2].

Collective cell migration can lead to moving cell fronts, which are routinely studied using *in vitro* cell biological experiments [7, 8]. These experiments often involve developing scratch assays, where an artificial gap, called a *scratch*, is created in a monolayer of cells [8]. Over a period of time, the cells move freely and randomly to close the gap [8]. In closing the gap, the cell front imitates healing an open wound [7]. Figure 1.1 illustrates a moving cell front in a scratch assay experiment.

Many studies construct mathematical models to describe moving cell fronts observed in scratch assay experiments [9–14]. As cells move freely and randomly in scratch assay experiments (Figure 1.1), their net migration is commonly described using the linear diffusion equation [1, 2]. Cells are also known to proliferate in scratch assay experiments [9,10,15]. The Fisher–Kolmogorov–Petrovsky–Piskunov model, also known as the Fisher-KPP model, extends the linear diffusion equation to include a logistic source term which describes cell proliferation [1, 16, 17]. The

Fisher-KPP model is a one dimensional, reaction–diffusion equation,

$$\frac{\partial c(x,t)}{\partial t} = \underbrace{D\frac{\partial^2 c(x,t)}{\partial x^2}}_{\text{diffusion}} + \underbrace{\lambda c(x,t)\left(1-\frac{c(x,t)}{K}\right)}_{\text{logistic source}}, \tag{1.1}$$

where $c(x,t) > 0$ is the cell density, $D > 0$ is the diffusion coefficient, $\lambda > 0$ is the proliferation rate, and $K > 0$ is the carrying capacity density [1, 16, 17].

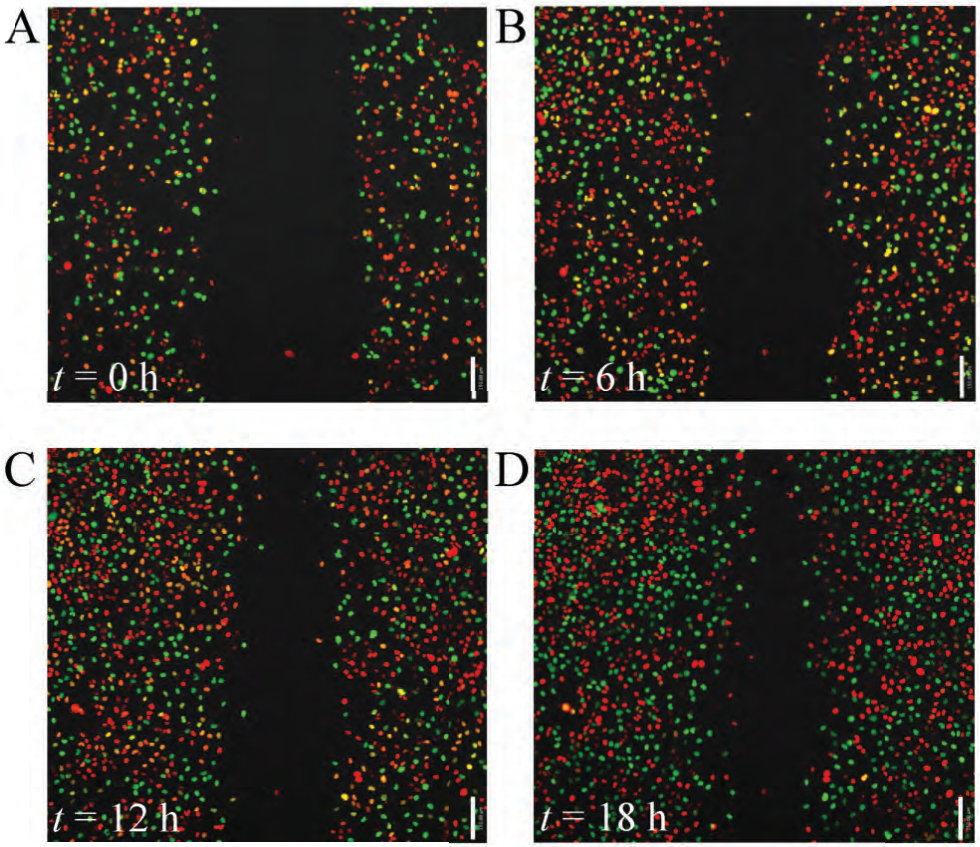

Figure 1.1: Experimental images of a scratch assay illustrating a moving cell front at $t = 0, 6, 12$ and 18 hours. The red, yellow and green colours indicate cells at different stages of the cell cycle. Reproduced from Vittadello et al. [9] with permission.

As the Fisher-KPP model captures the net migration and proliferation of cells, it is widely used in mathematical biology to describe collective cell behaviour. For example, the Fisher-KPP model is used to study moving cell fronts observed in scratch assay experiments [10, 13], as well as the development of tumours, such as glioblastoma [6, 18, 19]. Travelling wave solutions of the Fisher-KPP model are

commonly studied in mathematical biology [1, 2, 20–22], and can be interpreted in the context of wound healing [20, 22].

In this thesis, we take a different approach and consider a moving cell front in the context of epithelial tissues. Epithelial tissues are comprised of tightly packed layers of cells, and play an important role in wound healing and tumour development [23–25]. While Figure 1.1 illustrates that cells constantly exchange neighbours in scratch assay experiments, Figure 1.2 shows that the boundaries between neighbouring cells are maintained in epithelial tissues. As such, new reaction–diffusion equations are presented in this thesis to investigate the effect of cell boundaries on cell migration in epithelial tissues. In doing so, a free boundary is used to describe the moving cell front. This research takes the most fundamental approach and only considers the role of cell migration in a free boundary model of epithelial tissues. Cell proliferation is neglected, and could be considered one extension of this study.

1.1.2 Epithelial tissues

Epithelial tissues are layers of cells that form protective surfaces such as the skin and the lining of internal organs [23–25]. Figure 1.2(a)–(b) shows an epithelial tissue which lines the uterus. In such tissues, strong intercellular bonds between adjacent cells form tightly packed layers within the tissue [23, 26–28]. Epithelial tissues elastically deform by stretching or compressing in response to chemical signals and mechanical forces, or trauma, such as tumours and wounds [24, 27]. Tumours grow as cancerous cells invade healthy tissue, whereas wounds shrink as healthy cells migrate over the open wound. Thus, mathematical models are developed to study how epithelial tissues elastically deform due to tumour development, wound healing and morphogenesis.

Existing mathematical models typically use a mechanical spring model to capture the elasticity of epithelial tissues [29–31]. Figure 1.2(c) illustrates how a cross section of epithelial tissue relates to a series of interconnected mechanical springs. Bonds between adjacent cells [23, 26] are modelled by explicitly defining the cell boundaries. The mechanical spring model incorporates the effect of mechanical cell properties, such as resistance to deformation and cell size, on the shape of epithelial tissues. Mechanical forces can induce biochemical signals, such as intracellular signalling, which can cause the tissue to stretch or compress [32, 33]. In this thesis, cell–based mechanical properties are coupled to intracellular signalling to investigate their combined effect on the evolution of epithelial tissues. This is referred to as *mechanobiological* coupling.

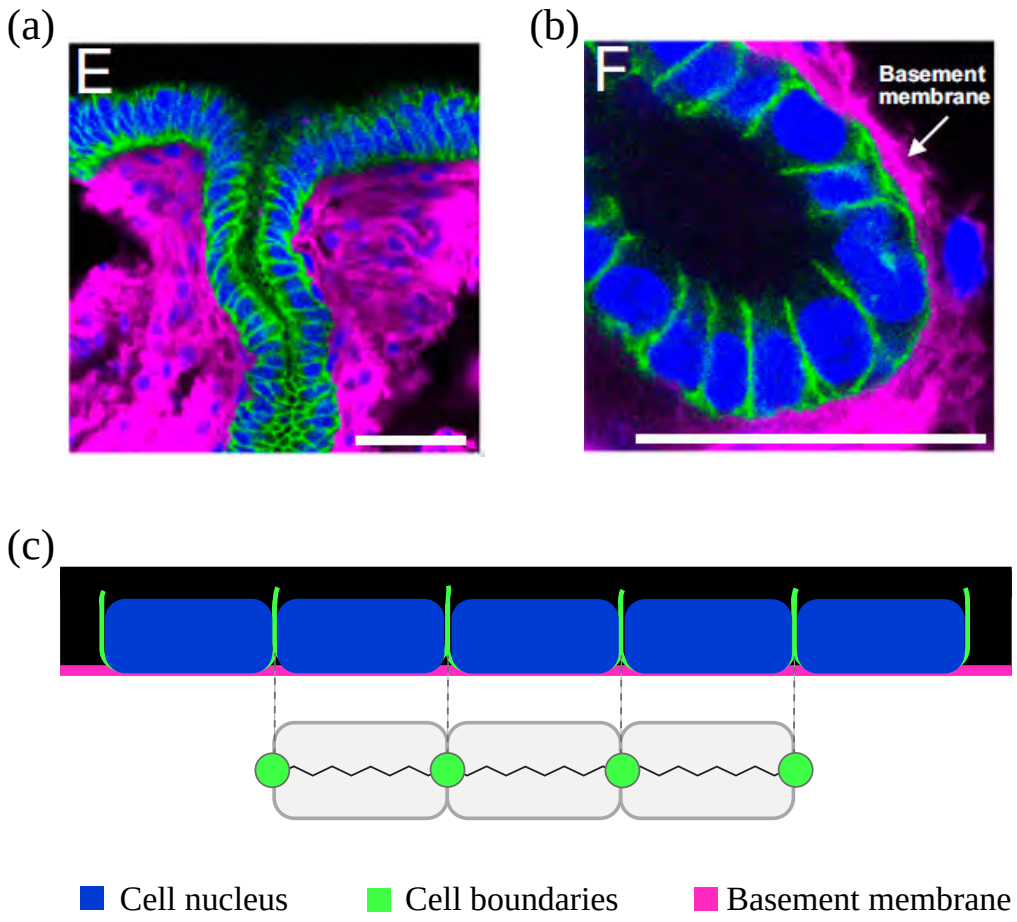

Figure 1.2: Experimental image of the lining of the uterus and corresponding model schematic. (a) shows a uterine epithelial tissue. The nucleus of individual cells is highlighted in blue, and the boundaries between adjacent cells is highlighted in green. The basement membrane is highlighted in magenta. A higher magnification of (a) is shown in (b). (c) illustrates a schematic of a one dimensional cross section of epithelial tissue and corresponding mechanical spring model. Experimental images in (a)–(b) are reproduced from [34] with permission.

1.1.3 Mathematical models

Mathematical models of epithelial tissues are broadly categorised as either discrete or continuum [29, 31]. Discrete models treat cells as individual discrete entities [35, 36]. Discrete models include cellular Potts models [37], cell–centre models [35] and cell–based models [29, 31]. Cell–based models represent cells as mechanical springs between cell boundaries, whereas cell–centre models represent cells by their centres. In this thesis, mechanobiological coupling is captured at the cell level in a cell–based discrete model. Figure 1.2(c) is an example of a cell–based model.

Discrete models capture cell–level information, such as elasticity, adhesion, motility and intracellular signalling [29,31,35,38], but often lack macroscopic behaviour [29]. In contrast, continuum models describe tissue–level behaviour, but provide no cell–level information [31]. A common continuum model is the linear diffusion equation which captures collective cell migration at the macroscopic level [1, 2]. Other continuum models, such as the Fisher-KPP model, consist of non-linear partial differential equations, and are more amenable to analysis than discrete models [16,17,29–31,38]. Possible analysis techniques for continuum models include linear stability analysis and travelling wave analysis [21, 39, 40].

A large number of continuum models are proposed without first considering cell–level information [32, 41–43]. For example, the Fisher-KPP model is a continuum model which suggests that collective cell migration and proliferation can be described by extending the linear diffusion equation to include a logistic source term [1,2]. While this model may reasonably reflect cell behaviour observed in cell biology experiments [9,10,12,13], it originates from considering how cell migration and proliferation effect cell behaviour at the macroscopic level, rather than individual cells at the microscopic level. However, a small number of continuum models are derived from a biologically–motivated discrete model using various coarse–graining techniques and assumptions [11, 29–31, 44]. One technique is to let the number of discrete entities (cells) tend to infinity [30, 31, 44]. Murphy et al. [29] develop a new technique by assuming that each individual cell consists of multiple identical springs. To construct the continuum model, Murphy et al. [29] let the number of springs per cell tend to infinity while maintaining a constant number of cells. In this thesis, the continuum model is derived by letting the number of cells tend to infinity. Our focus in deriving the continuum model is to investigate how cell–level mechanisms, such as intracellular signalling, relate to tissue–level behaviour.

Epithelial tissues play important roles in tumour development, wound healing and morphogenesis [26, 27, 45, 46]. Temporal variation in tumour size and wound width can be thought of as the evolution of a free boundary [47]. Existing free boundary models which study tumour development and wound healing are reviewed in [47]. Many continuum free boundary models pre-specify the rate of tissue elongation to match experimental observations [48–52]. Other continuum models describe the evolution of the free boundary using a classical one–phase Stefan condition [53,54]. In some continuum models which consider tumour spheroids, the evolution of the free boundary depends on the local nutrient concentration [55–57]. In this thesis, a free boundary is incorporated in the discrete and continuum models to study the effect of mechanobiological coupling on the

evolution of epithelial tissues. By presenting the continuum limit description of a biologically–motivated discrete model, a novel free boundary condition is derived which reflects the mechanobiological coupling and biological mechanisms included in the discrete model.

1.1.4 Modelling mechanical and chemical cell properties

Many models in mathematical biology treat biological tissues and groups of cells as homogeneous, where each cell is assumed to be identical and possess the same cellular properties [13, 30, 31, 53]. However, biological tissues are naturally heterogeneous as cells can be distinguished by distinct properties, such as cell size or cell age [25]. Experimental images in Figure 1.1 illustrate that cells in scratch assay experiments can be distinguished by their stage within the cell cycle. In addition, Figure 1.2(a)–(b) shows that epithelial tissues contain cells with various sizes and shapes. Heterogeneity can also arise due disease progression and result in malignant tissues [58, 59]. Some models capture heterogeneity as spatial and temporal variation in mechanical and chemical cell properties to differentiate between cells [29, 60]. Under certain conditions, models which consider heterogeneous cell populations are also applicable to homogeneous cell populations [29]. As models which consider homogeneous cell populations assume cells possess identical cellular properties [30, 31], these models are not applicable to heterogeneous cell populations.

Some models investigate the role of purely mechanical cell properties on epithelial tissue behaviour [29–31, 61, 62]. Baker et al. [30] consider mechanical cell properties in a free boundary model for homogeneous cell populations. Murphy et al. [29] investigate the role of mechanical heterogeneity in tissues of fixed length. By including mechanobiological coupling, the free boundary model developed in this thesis is applicable to heterogeneous cell populations. Thus, the work of Baker et al. [30] and Murphy et al. [29] is unified and extended.

Other studies investigate the role of chemical cell properties on the shape of epithelial cells [35, 43, 60, 63]. For example, Smith et al. [63] consider how chemical signalling influences the growth rate of cells, whereas Zmurchok et al. [60] couple cellular tension and chemical cell properties. Zmurchok et al. [60] finds that depending on the strength of the coupling, the cell either mechanically relaxes, or continuously expands and contracts. This is referred to as non-oscillatory and oscillatory dynamics. In this research, the work of Zmurchok et al. [60] is extended by investigating how oscillatory and non-oscillatory tissue dynamics arise due to mechanobiological coupling.

1.1.5 Modelling mechanobiological coupling

To confirm the accuracy of the continuum model developed in this thesis, including the free boundary condition, we compare solutions of the discrete and continuum models relating to different biological scenarios and signalling pathways. First, the work of Baker et al. [30] is replicated by considering a homogeneous tissue, where the mechanical properties of cells are constant and independent of the chemical properties. To investigate mechanobiological coupling in epithelial tissues, the model is applied in two case studies. The first case study considers the Rac–Rho pathway where diffusible chemicals called Rho GTPases regulate the shape of epithelial cells [60, 64–69]. Additionally, Rho GTPases play a role in tumour development by contributing to the survival and migration of diseased cells in healthy tissues [70,71]. Zmurchok et al. [60] investigates how the Rac–Rho pathway leads to oscillatory and non-oscillatory dynamics in a solely discrete modelling framework. The results of this study are extended in the current research by including mechanobiological coupling in both a discrete and continuum modelling framework. In doing so, we investigate how mechanobiological coupling leads to oscillatory and non-oscillatory tissue dynamics.

The second case study involves an activator–inhibitor system in the context of Turing patterns [1]. The skin of marine angelfish exhibit a striped pattern that dynamically changes as the animal grows [72]. Kondo et al. [72] propose a reaction–diffusion mechanism to account for spatial and temporal variation in the pattern as the skin evolves. Previous mathematical studies exclusively use continuum models to investigate the development of spatial–temporal patterns [51,52,73,74]. These studies model the skin as a uniformly evolving cellular domain [51,52,73,74]. We extend these studies by investigating the development of spatial–temporal patters in both a discrete and continuum modelling framework. As the biological mechanisms included in the discrete model naturally gives rise to non-uniform tissue evolution, the skin is modelled as a non-uniformly evolving cellular domain.

1.1.6 Aims

The work presented in this thesis aims to:

1. investigate mechanobiological coupling in epithelial tissues;

2. develop and solve a free boundary mechanobiological model of epithelial tissues in both a discrete and continuum modelling framework; and

3. determine the accuracy of the continuum model by comparing numerical solutions of the discrete and continuum models.

In achieving these aims, the evolution of epithelial tissues in response to mechanobiological coupling is investigated, and the findings of previous studies are extended.

1.2 Thesis structure

This thesis is comprised of two main chapters. Chapter 2 is the main document of a preprint which is under review at *Proceedings of the Royal Society A: Mathematical, Physical and Engineering Sciences*. Chapter 3 is the accompanying supplementary material. The preprint is available on bioRxiv.

In Chapter 2, a novel free boundary mechanobiological model for epithelial tissues is developed. Mechanobiological coupling is introduced at the cell level, and new reaction–diffusions equations are derived to describe tissue–level outcomes. In taking the continuum limit description of the discrete model, a novel free boundary condition is derived that corresponds to the underlying biological mechanisms and heterogeneity included in the discrete model. To determine the accuracy of the continuum model, the work of Baker et al. [30] is replicated, and the role of mechanobiological coupling is considered in two case studies. The first case study considers the Rac–Rho pathway, and investigates how mechanobiological coupling leads to oscillatory and non-oscillatory tissue dynamics. The second case study considers an activator–inhibitor system in the context of Turing patterns on a non-uniformly evolving cellular domain.

Chapter 3 outlines the numerical methods for the free boundary model developed in Chapter 2, and presents additional numerical simulations. The numerical methods of the discrete and continuum models are outlined in detail. Additional numerical results are presented which support the case studies in Chapter 2. These include analysing long time tissue behaviour, and additional comparisons of discrete and continuum solutions. The methodology used to determine the model parameters which give rise to oscillatory and non-oscillatory tissue dynamics is also outlined. This involves phase plane and linear stability analysis.

Chapter 4 summarises the key findings presented in this thesis, and discusses opportunities for future research.

1.3 Statement of joint authorship

This section outlines the contribution of the Masters candidate and the co-authors of the joint publication presented in this thesis.

Chapter 2: A free boundary mechanobiological model of epithelial tissues

This chapter is the main document of the preprint entitled "A free boundary mechanobiological model of epithelial tissues". This preprint is available on bioRxiv, and is under review at *Proceedings of the Royal Society A: Mathematical, Physical and Engineering Sciences*. The contribution of each co-author is listed below.

- **Tamara A. Tambyah** devised the methodology, developed the models, performed all numerical simulations, conducted the analysis, generated the figures and drafted the preprint for submission.
- Ryan J. Murphy assisted with numerical simulations and critically reviewed the preprint for submission.
- Pascal R. Buenzli supervised the analysis and generation of the figures, and critically reviewed the preprint for submission.
- Matthew J. Simpson initiated the theoretical concepts, supervised the analysis and generation of the figures, and critically reviewed the preprint for submission.

Chapter 3: Mathematical techniques for a free boundary mechanobiological model of epithelial tissues

This chapter is the supplementary material of the preprint entitled "A free boundary mechanobiological model of epithelial tissues". This preprint is available on bioRxiv, and under review at *Proceedings of the Royal Society A: Mathematical, Physical and Engineering Sciences*. The contribution of each co-author is listed below.

- **Tamara A. Tambyah** implemented the mathematical techniques, performed analysis, generated the figures and drafted the preprint for submission.
- Ryan J. Murphy critically reviewed the preprint for submission.
- Pascal R. Buenzli supervised the analysis and generation of the figures, and critically reviewed the preprint for submission.

- Matthew J. Simpson supervised the analysis and generation of the figures, and critically reviewed the preprint for submission.

Chapter 2

A free boundary mechanobiological model of epithelial tissues

This chapter comprises of the main document of a preprint available on bioRxiv. This preprint is under review at *Proceedings of the Royal Society A: Mathematical, Physical and Engineering Sciences* as:

A free boundary mechanobiological model of epithelial tissues

Tamara A. Tambyah, Ryan J. Murphy, Pascal R. Buenzli and Matthew J. Simpson

2.1 Introduction

Epithelial tissues consist of tightly packed monolayers of cells [27, 28, 44]. Mechanical cell properties, such as resistance to deformation and cell size, and chemical cell properties, such as intracellular signalling, impact the shape of epithelial tissues [27, 32]. The role of purely mechanical cell properties on tissue dynamics has been studied using mathematical and computational models [29–31, 38, 61, 62]. Other models focus on intracellular signalling to examine how chemical signalling affects tissue dynamics. [35, 43, 60, 63, 75]. We extend these studies by developing a model which couples mechanical cell properties to intracellular signalling. We refer to this as *mechanobiological* coupling. By including mechanobiological coupling in a discrete computational framework, new reaction–diffusion equations are derived to describe how cell–level mechanisms relate to tissue–level outcomes.

Epithelial tissues play important roles in cancer development, wound healing and morphogenesis [27, 45, 46]. Temporal changes in tumour size and wound width in epithelial monolayers can be thought of as the evolution of a free boundary [47, 76]. Many free boundary models use a classical one–phase Stefan condition to describe the evolution of the free boundary [53, 54]. Other free boundary models, particularly those used to study biological development, pre-specify the rate of tissue elongation to match experimental observations [48–52, 73, 74]. In this study, we take a different approach by constructing the continuum limit description of a biologically–motivated discrete model. In doing so, we derive a novel free boundary condition that arises from the underlying biological mechanisms included in the discrete model. While the discrete model is suitable for describing cell–level observations and phenomena [35, 36], the continuum limit description is suitable to describe tissue–level dynamics and is more amenable to analysis [39, 40, 77].

To confirm the accuracy of the continuum limit description, including the new free boundary condition, we compare the solution of the discrete model with the solution of the continuum model for a homogeneous tissue with no mechanobiological coupling, and observe good correspondence. To investigate mechanobiological coupling within epithelial tissues, the modelling framework is applied in two different case studies. The first case study involves the Rac–Rho pathway where diffusible chemicals called Rho GTPases regulate mechanical cell properties [60, 64–69]. We explicitly consider how the coupling between diffusible chemical signals and mechanical properties lead to different tissue–level outcomes, including oscillatory and non-oscillatory tissue dynamics. The second case study involves the diffusion

and reaction of an activator–inhibitor system in the context of Turing patterns on a non-uniformly evolving cellular domain [52, 73, 74]. In both case studies, the numerical solution of the continuum model provides an accurate description of the underlying discrete mechanisms.

2.2 Model Description

In this section, we first describe the cell–based model, referred to as the *discrete model*, where mechanical cellular properties are coupled with intracellular signalling. To provide mathematical insight into the discrete model, we then derive the corresponding coarse–grained approximation, which is referred to as the *continuum model*.

2.2.1 Discrete model

To represent a one dimensional (1D) cross section of epithelial tissue, a 1D chain of cells is considered [31, 61] (Figure 2.1). The tissue length, $L(t)$, evolves in time, while the number of cells, N, remains fixed. We define $x_i(t)$, $i = 0, 1, \dots N$, to represent the cell boundaries, such that the left boundary of cell i is $x_{i-1}(t)$ and the right boundary of cell i is $x_i(t)$. The left tissue boundary is fixed at $x_0(t) = 0$ and $x_N(t) = L(t)$ is a free boundary.

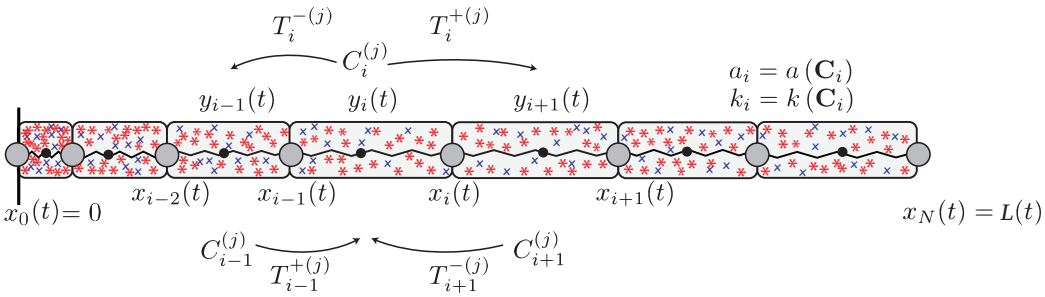

Figure 2.1: Schematic of the discrete model where mechanical cell properties, a_i and k_i, are functions of the family of chemical signals, $\mathbf{C}_i(t)$. In this schematic we consider two diffusing chemical species where the concentration in the i^{th} cell is $\mathbf{C}_i(t) = \left\{C_i^{(1)}(t), C_i^{(2)}(t)\right\}$. The diffusive flux into cell i from cells $i \pm 1$, and the diffusive flux out of cell i into cells $i \pm 1$ is shown. Cell i, with boundaries at $x_{i-1}(t)$ and $x_i(t)$, is associated with a resident point, $y_i(t)$, that determines the diffusive transport rates, $T_i^{\pm(j)}$.

Each cell, which we consider to be a mechanical spring [31, 61], is assigned potentially distinct mechanical properties, a_i and k_i, such that the resulting tissue is

heterogeneous (Figure 2.1) [38]. Each cell i contains a family of well mixed chemical species, $\mathbf{C}_i(t) = \left\{C_i^{(1)}(t), C_i^{(2)}(t), \ldots, C_i^{(m)}(t)\right\}$, where $C_i^{(j)}(t)$ represents the concentration of the j^{th} chemical species in cell i at time t. As the cell boundaries evolve with time, $C_i^{(j)}(t)$ tends to decrease as cell i expands. Conversely, $C_i^{(j)}(t)$ tends to increase as cell i compresses. Furthermore, $C_i^{(j)}(t)$ diffuses from cell i to cells $i \pm 1$. The mechanical properties of individual cells, such as the cell resting length, $a_i = a\left(\mathbf{C}_i\right)$, and the cell stiffness, $k_i = k\left(\mathbf{C}_i\right)$, may depend on the local chemical concentration, $\mathbf{C}_i(t)$. We refer to this as mechanobiological coupling.

As cells move in overdamped, viscous environments [29, 38, 78], the location of each cell boundary i evolves as

$$\eta \frac{\mathrm{d}x_i}{\mathrm{d}t} = f_{i+1} - f_i, \qquad i = 1, 2, \ldots, N-1, \tag{2.1}$$

where $\eta > 0$ is the mobility coefficient, and f_i is the cell-to-cell interaction force acting on cell boundary i from the left [29, 38]. For simplicity, we choose a linear, Hookean force law given by

$$f_i = k\left(\mathbf{C}_i\right)\left(x_i(t) - x_{i-1}(t) - a\left(\mathbf{C}_i\right)\right), \qquad i = 1, 2, \ldots, N. \tag{2.2}$$

The fixed boundary at $x_0(t) = 0$ has zero velocity, whereas the free boundary at $x_N(t) = L(t)$ moves solely due to the force acting from the left:

$$\eta \frac{\mathrm{d}x_0}{\mathrm{d}t} = 0, \qquad \eta \frac{\mathrm{d}x_N}{\mathrm{d}t} = -f_N. \tag{2.3}$$

We now formulate a system of ordinary differential equations (ODEs) that describe the rate of change of $C_i^{(j)}(t)$ due to changes in cell length and diffusive transport. A position–jump process is used to describe the diffusive transport of $C_i^{(j)}(t)$. We use $T_i^{\pm(j)}$ to denote the rate of diffusive transport of $C_i^{(j)}(t)$ from cell i to cells $i \pm 1$, respectively [79, 80] (Figure 2.1). For a standard unbiased position–jump process with a uniform spatial discretisation, linear diffusion at the macroscopic scale is obtained by choosing constant $T_i^{\pm(j)}$ [79]. As the cell boundaries evolve with time, one way to interpret $C_i^{(j)}(t)$ is that it represents a time–dependent, non-uniform spatial discretisation of the concentration profile over the chain of cells. Therefore, care must be taken to specify $T_i^{\pm(j)}$ on the temporally evolving spatial discretisation if we suppose the position–jump process corresponds to linear diffusion at the macroscopic level [80].

Yates et al. [80] show that in order for the position–jump process to lead to linear diffusion at the macroscopic level, the length– and time–dependent transport

rates must be chosen as

$$T_i^{-(j)} = \frac{2D_j}{(y_i(t) - y_{i-1}(t))\,(y_{i+1}(t) - y_{i-1}(t))}, \qquad i = 2, \ldots, N-1, \tag{2.4}$$

$$T_i^{+(j)} = \frac{2D_j}{(y_{i+1}(t) - y_i(t))\,(y_{i+1}(t) - y_{i-1}(t))}, \qquad i = 2, \ldots, N-1, \tag{2.5}$$

where $D_j > 0$ is the diffusion coefficient of the j^{th} chemical species at the macroscopic level, and $y_i(t)$ is the *resident point* associated with cell i (Figure 2.1) [80]. The resident points are a Voronoi partition such that the left jump length for the transport of $C_i^{(j)}(t)$ is $y_i(t) - y_{i-1}(t)$, and the right jump length for the transport of $C_i^{(j)}(t)$ is $y_{i+1}(t) - y_i(t)$ [80]. Complete details of defining a Voronoi partition are outlined in Chapter 3.2.1.

At the tissue boundaries, we set $T_1^{-(j)} = T_N^{+(j)} = 0$ so that the flux of $C_1^{(j)}(t)$ and $C_N^{(j)}(t)$ across $x_0(t) = 0$ and $x_N(t) = L(t)$ is zero. We follow Yates et al. [80] and choose the inward jump length for the transport of $C_1^{(j)}(t)$ and $C_N^{(j)}(t)$ as $2\,(y_1(t) - x_0(t))$ and $2\,(x_N(t) - y_N(t))$, respectively, giving

$$T_1^{+(j)} = \frac{2D_j}{(y_2(t) - y_1(t))\,(y_2(t) + y_1(t))}, \tag{2.6}$$

$$T_N^{-(j)} = \frac{2D_j}{(y_N(t) - y_{N-1}(t))\,(x_N(t) - y_N(t) - y_{N-1}(t))}. \tag{2.7}$$

Therefore, the ODEs which describe the evolution of $C_i^{(j)}(t)$ are:

$$\frac{\mathrm{d}C_1^{(j)}}{\mathrm{d}t} = \underbrace{Z^{(j)}\left(\mathbf{C}_1\right)}_{\substack{\text{chemical}\\ \text{reactions}}} - \underbrace{\frac{C_1^{(j)}}{l_1}\frac{\mathrm{d}l_1}{\mathrm{d}t}}_{\substack{\text{changes in}\\ \text{cell length}}} + \frac{1}{l_1}\left(\underbrace{T_2^{-(j)}C_2^{(j)}l_2}_{\substack{\text{diffusion into}\\ \text{cell 1}}} - \underbrace{T_1^{+(j)}C_1^{(j)}l_1}_{\substack{\text{diffusion out of}\\ \text{cell 1}}}\right), \tag{2.8}$$

$$\begin{aligned}\frac{\mathrm{d}C_i^{(j)}}{\mathrm{d}t} &= \underbrace{Z^{(j)}\left(\mathbf{C}_i\right)}_{\substack{\text{chemical}\\ \text{reactions}}} - \underbrace{\frac{C_i^{(j)}}{l_i}\frac{\mathrm{d}l_i}{\mathrm{d}t}}_{\substack{\text{changes in}\\ \text{cell length}}} \\ &+ \frac{1}{l_i}\left(\underbrace{T_{i-1}^{+(j)}C_{i-1}^{(j)}l_{i-1} + T_{i+1}^{-(j)}C_{i+1}^{(j)}l_{i+1}}_{\text{diffusion into cell } i} - \underbrace{\left(T_i^{+(j)} + T_i^{-(j)}\right)C_i^{(j)}l_i}_{\text{diffusion out of cell } i}\right),\end{aligned} \tag{2.9}$$

$$i = 2, \ldots, N-1,$$

$$\frac{\mathrm{d}C_N^{(j)}}{\mathrm{d}t} = \underbrace{Z^{(j)}\left(\mathbf{C}_N\right)}_{\substack{\text{chemical}\\ \text{reactions}}} - \underbrace{\frac{C_N^{(j)}}{l_N}\frac{\mathrm{d}l_N}{\mathrm{d}t}}_{\substack{\text{changes in}\\ \text{cell length}}} + \frac{1}{l_N}\left(\underbrace{T_{N-1}^{+(j)}C_{N-1}^{(j)}l_{N-1}}_{\substack{\text{diffusion into}\\ \text{cell } N}} - \underbrace{T_N^{-(j)}C_N^{(j)}l_N}_{\substack{\text{diffusion out of}\\ \text{cell } N}}\right), \tag{2.10}$$

where $l_i = x_i(t) - x_{i-1}(t)$ is the length of cell i. Chemical reactions among the chemical species residing in the i^{th} cell are described by $Z^{(j)}(\mathbf{C}_i)$. The form of $Z^{(j)}(\mathbf{C}_i)$ is chosen to correspond to different signalling pathways.

In summary, the discrete model is given by Equations (2.1)–(2.10), where Equations (2.1)–(2.3) describe the mechanical interaction of cells, and Equations (2.8)–(2.10) describe the underlying biological mechanisms. We solve this deterministic system of ODEs numerically using `ode15s` in MATLAB [81]. The numerical method is outlined in Chapter 3.2.1, and key numerical algorithms to solve the discrete model are available on GitHub.

2.2.2 Continuum model

Assuming that the tissue consists of a sufficiently large number of cells, N, we now derive an approximate continuum limit description of the discrete model. In the discrete model, $i = 0, 1, \ldots, N$ is a discrete variable which indexes cell positions and cell properties. The time evolution of the cell boundaries, $x_i(t)$, is a set of $N + 1$ discrete functions that depend continuously upon time. In contrast, the continuum model describes the spatially continuous evolution of cell boundary trajectories in terms of the cell density per unit length, $q(x, t)$. In the continuum model, $\bar{i} = i/N$ is the continuous analogue of i [30]. As $N \to \infty$, $\bar{i} = 0, 1/N, \ldots, 1$ becomes a continuous variable and defines a continuum of cells. The spatially and temporally continuous cell density is [30, 31]

$$q(x,t) = N\frac{\partial \bar{i}(x,t)}{\partial x}, \qquad x \in [0, L(t)] \text{ and } \bar{i} \in [0,1]. \tag{2.11}$$

At any time t, $x(\bar{i}, t)$ is the inverse function of $\bar{i}(x, t)$ where $x \in [0, L(t)]$ for $\bar{i} \in [0, 1]$. We use $x(\bar{i}, t)$ to represent the continuous spatial and temporal evolution of cell boundary trajectories [30].

The discrete quantity $\mathbf{C}_i(t)$ is represented by a multicomponent vector field in the continuum model, $\boldsymbol{\mathcal{C}}(x, t) = \{\mathcal{C}_1(x, t), \mathcal{C}_2(x, t), \ldots, \mathcal{C}_m(x, t)\}$. Assuming that the mechanical relaxation of cells is sufficiently fast such that the spatial distribution of cell lengths is slowly varying in space [29], the location of the resident points can be approximated as the midpoint of each cell,

$$\mathcal{C}_j\left(x\left(\frac{i}{N} - \frac{1}{2N}, t\right), t\right) = C_i^{(j)}(t), \qquad i = 1, \ldots, N. \tag{2.12}$$

In Equation (2.12), the subscript j denotes the j^{th} chemical species in the continuum model, and the superscript (j) denotes the j^{th} chemical species in the

discrete analogue. Mechanobiological coupling is introduced by allowing the cell stiffness, $k(\boldsymbol{\mathcal{C}})$, and the cell resting length, $a(\boldsymbol{\mathcal{C}})$, to depend on the local chemical concentration.

We write the linear force law for the continuum of cells as

$$f(\bar{i},t) = k(\boldsymbol{\mathcal{C}})\left(x(\bar{i},t) - x(\bar{i}-1/N,t) - a(\boldsymbol{\mathcal{C}})\right), \tag{2.13}$$

where $\boldsymbol{\mathcal{C}}$ is evaluated at $\bar{i}-1/(2N)$. Thus, the equations of motion are:

$$\eta\frac{\partial x(\bar{i},t)}{\partial t} = 0, \qquad \bar{i}=0, \tag{2.14}$$

$$\eta\frac{\partial x(\bar{i},t)}{\partial t} = f(\bar{i}+1/N,t) - f(\bar{i},t), \qquad \bar{i}\in(1/N,1), \tag{2.15}$$

$$\eta\frac{\partial x(\bar{i},t)}{\partial t} = -f(\bar{i},t), \qquad \bar{i}=1. \tag{2.16}$$

The definition of $f(\bar{i},t)$ in Equation (2.13) contains arguments evaluated at $\bar{i}$, $\bar{i}-1/N$ and $\bar{i}-1/(2N)$. Substituting Equation (2.13) into Equations (2.14)–(2.16), and expanding all terms in a Taylor series about $\bar{i}$ gives,

$$\eta\frac{\partial x}{\partial t} = 0, \qquad \bar{i}=0, \tag{2.17}$$

$$\eta\frac{\partial x}{\partial t} = -\frac{a}{N}\frac{\partial k}{\partial \bar{i}} - \frac{k}{N}\frac{\partial a}{\partial \bar{i}} + \frac{1}{N^2}\frac{\partial x}{\partial \bar{i}}\frac{\partial k}{\partial \bar{i}} + \frac{k}{N^2}\frac{\partial^2 x}{\partial \bar{i}^2} + \mathcal{O}\left(N^{-3}\right), \qquad \bar{i}\in(1/N,1), \tag{2.18}$$

$$\eta\frac{\partial x}{\partial t} = ak - \frac{k}{N}\frac{\partial x}{\partial \bar{i}} - \frac{k}{2N}\frac{\partial a}{\partial \bar{i}} - \frac{a}{2N}\frac{\partial k}{\partial \bar{i}} + \frac{1}{2N^2}\frac{\partial k}{\partial \bar{i}}\frac{\partial x}{\partial \bar{i}} + \frac{k}{2N^2}\frac{\partial^2 x}{\partial \bar{i}^2} + \frac{k}{4N^2}\frac{\partial^2 a}{\partial \bar{i}^2} + \frac{a}{4N^2}\frac{\partial^2 k}{\partial \bar{i}^2} + \frac{1}{4N^2}\frac{\partial k}{\partial \bar{i}}\frac{\partial a}{\partial \bar{i}} + \mathcal{O}\left(N^{-3}\right), \qquad \bar{i}=1. \tag{2.19}$$

To describe the continuous evolution of cell trajectories and cell properties, we write $1/q(x,t) = x(\bar{i},t) - x(\bar{i}-1/N,t)$ [29, 38], and define the continuous linear force law corresponding to Equation (2.13) as a 1D stress field,

$$f(x,t) = k(\boldsymbol{\mathcal{C}}(x,t))\left(\frac{1}{q(x,t)} - a(\boldsymbol{\mathcal{C}}(x,t))\right), \qquad x\in(0,L(t)). \tag{2.20}$$

We express Equations (2.17)–(2.19) in terms of $q(x,t)$ and $f(x,t)$ through a change of variables from $(\bar{i},t)$ to (x,t) [30, 31]. The change of variables gives

$$\frac{\partial x}{\partial \bar{i}} = \frac{N}{q}, \qquad \frac{\partial x}{\partial t} = -\frac{N}{q}\frac{\partial \bar{i}}{\partial t}, \tag{2.21}$$

$$\frac{\partial k}{\partial \bar{i}} = \frac{\partial k}{\partial x}\frac{\partial x}{\partial \bar{i}} = \frac{N}{q}\frac{\partial k}{\partial x}, \qquad \frac{\partial a}{\partial \bar{i}} = \frac{\partial a}{\partial x}\frac{\partial x}{\partial \bar{i}} = \frac{N}{q}\frac{\partial a}{\partial x}. \tag{2.22}$$

Complete details of the change of variables calculation are outlined in Chapter 3.1.1.

The local cell velocity, $u(x,t) = \partial x/\partial t$, is derived by substituting Equations (2.21)–(2.22) into the right hand side of Equation (2.18). Factorising in terms of $f(x,t)$ gives,

$$u(x,t) = \frac{1}{\eta q(x,t)} \frac{\partial f(x,t)}{\partial x}, \qquad x \in (0, L(t)). \tag{2.23}$$

As $u(x,t) = \partial x/\partial t$, we substitute Equation (2.21) into the left hand side of Equation (2.23) to derive the governing equation for cell density. The resulting equation is differentiated with respect to x to give,

$$\frac{\partial}{\partial x}\left(N\frac{\partial \bar{i}}{\partial t}\right) = \frac{\partial}{\partial x}\left(-\frac{1}{\eta}\frac{\partial f(x,t)}{\partial x}\right), \qquad x \in (0, L(t)). \tag{2.24}$$

The order of differentiation on the left hand side of Equation (2.24) is reversed, and Equation (2.21) is used [30, 31] to give,

$$\frac{\partial q(x,t)}{\partial t} = -\frac{1}{\eta}\frac{\partial^2 f(x,t)}{\partial x^2}, \qquad x \in (0, L(t)). \tag{2.25}$$

The boundary condition for the evolution of $L(t)$ is obtained by substituting Equations (2.21)–(2.22) into the right hand side of Equation (2.19), giving

$$\begin{aligned} \eta \frac{\partial x}{\partial t} &= ak - \frac{k}{q} - \frac{k}{2q^3}\frac{\partial q}{\partial x} + \frac{1}{2q^2}\frac{\partial k}{\partial x} - \frac{1}{2q}\frac{\partial}{\partial x}(ak) \\ &\quad + \frac{1}{4q}\left\{\frac{1}{q}\frac{\partial a}{\partial x}\frac{\partial k}{\partial x} + k\frac{\partial}{\partial x}\left(\frac{1}{q}\frac{\partial a}{\partial x}\right) + a\frac{\partial}{\partial x}\left(\frac{1}{q}\frac{\partial k}{\partial x}\right)\right\}, \qquad x = L(t). \end{aligned} \tag{2.26}$$

As $u(x,t) = \partial x/\partial t$, the left hand side of Equation (2.26) is equated to Equation (2.23). Factorising in terms of $f(x,t)$ gives the free boundary condition

$$\begin{aligned} 0 = f(x,t) &+ \frac{1}{2q(x,t)}\frac{\partial f(x,t)}{\partial x} + \frac{1}{4q(x,t)}\left\{\frac{1}{q(x,t)}\frac{\partial a\left(\boldsymbol{\mathcal{C}}(x,t)\right)}{\partial x}\frac{\partial k\left(\boldsymbol{\mathcal{C}}(x,t)\right)}{\partial x}\right. \\ &+ k\left(\boldsymbol{\mathcal{C}}(x,t)\right)\frac{\partial}{\partial x}\left(\frac{1}{q(x,t)}\frac{\partial a\left(\boldsymbol{\mathcal{C}}(x,t)\right)}{\partial x}\right) \\ &\left.+ a\left(\boldsymbol{\mathcal{C}}(x,t)\right)\frac{\partial}{\partial x}\left(\frac{1}{q(x,t)}\frac{\partial k\left(\boldsymbol{\mathcal{C}}(x,t)\right)}{\partial x}\right)\right\}, \qquad x = L(t). \end{aligned} \tag{2.27}$$

A similar transformation is applied to Equation (2.17) to yield the left boundary

condition as

$$\frac{\partial f(x,t)}{\partial x} = 0, \qquad\qquad x = 0. \tag{2.28}$$

Equations (2.23), (2.25), (2.27) and (2.28) form a continuum limit approximation of the discrete model. Equations (2.23), (2.25) and (2.28) were reported previously by Murphy et al. [29] who consider heterogeneous tissues of fixed length without mechanobiological coupling. A key contribution here is the derivation of Equation (2.27), which describes how the free boundary evolves due to the underlying biological mechanisms and heterogeneity included in the discrete model. For a homogeneous tissue where the cell stiffness and cell resting length are constant and independent of $\mathcal{C}_j(x,t)$, Equation (2.27) is equivalent to Equation (23) in Baker et al. [30]. Chapter 3.1.2 shows that Equations (2.23), (2.25) and (2.28) can be derived without expanding all components of Equations (2.14)–(2.15). As the definition of $f(\bar{i},t)$ in Equation (2.13) contains arguments evaluated at $\bar{i}$, $\bar{i}-1/N$ and $\bar{i}-1/(2N)$, it is necessary to expand all components of Equation (2.16) about $\bar{i}$ to derive Equation (2.27). For consistency, Equations (2.23), (2.25) and (2.28) are derived in the same way.

We now consider a reaction–diffusion equation for the evolution of $\mathcal{C}_j(x,t)$. The reaction–diffusion equation involves terms associated with the material derivative, diffusive transport, and source terms that reflect chemical reactions as well as the effects of changes in cell length,

$$\begin{aligned} &\underbrace{\frac{\partial \mathcal{C}_j(x,t)}{\partial t} + u(x,t)\frac{\partial \mathcal{C}_j(x,t)}{\partial x}}_{\text{material derivative}} + \underbrace{\mathcal{C}_j(x,t)\frac{\partial u(x,t)}{\partial x}}_{\text{changes in cell length}} \\ &\qquad - \underbrace{D_j \frac{\partial^2 \mathcal{C}_j(x,t)}{\partial x^2}}_{\text{diffusion}} = \underbrace{Z_j\left(\boldsymbol{\mathcal{C}}\left(x,t\right)\right)}_{\text{chemical reactions}}, \qquad\qquad x \in \left(0, L(t)\right). \end{aligned} \tag{2.29}$$

The material derivative arises from differentiating Equation (2.12) with respect to time, and describes to the propagation of cell properties along cell boundary characteristics [29, 38]. The term describing the effects of changes in cell length arises directly from the discrete mechanisms described in Equations (2.8)–(2.10). The linear diffusion term arises due to the choice of jump rates in Equations (2.4)–(2.7) of the discrete model [80]. Chemical reactions are described by $Z_j\left(\boldsymbol{\mathcal{C}}\left(x,t\right)\right)$, and originate from equivalent terms in the discrete model, $Z^{(j)}\left(\mathbf{C}_i\right)$.

Boundary conditions for $\mathcal{C}_j(x,t)$ are chosen to ensure mass is conserved at $x=0$ and $x=L(t)$. As the left tissue boundary is fixed, we set $\partial \mathcal{C}_j/\partial x = 0$ at $x=0$. At $x=L(t)$, we enforce that the total flux of $\mathcal{C}_j(x,t)$ in the frame of reference

co-moving with the right tissue boundary is zero for all time,

$$\underbrace{u\left(L(t),t\right)\mathcal{C}_j\left(L(t),t\right)-D_j\frac{\partial\mathcal{C}_j\left(L(t),t\right)}{\partial x}}_{\text{total flux at } x=L(t)}-\underbrace{u\left(L(t),t\right)\mathcal{C}_j(L(t),t)}_{\text{moving frame of reference}}=0, \tag{2.30}$$

where $u\left(L(t),t\right)=\mathrm{d}L/\mathrm{d}t$. Thus, $\partial\mathcal{C}_j/\partial x=0$ at $x=L(t)$. Writing Equation (2.29) in conservative form gives,

$$\frac{\partial q(x,t)}{\partial t}=-\frac{1}{\eta}\frac{\partial^2 f(x,t)}{\partial x^2}, \qquad x\in\left(0,L\left(t\right)\right), \tag{2.31}$$

$$\begin{aligned}\frac{\partial\mathcal{C}_j(x,t)}{\partial t}+\frac{\partial}{\partial x}\left(u(x,t)\mathcal{C}_j(x,t)-D_j\frac{\partial\mathcal{C}_j\left(x,t\right)}{\partial x}\right)\\ =Z_j\left(\boldsymbol{\mathcal{C}}\left(x,t\right)\right), \qquad x\in\left(0,L\left(t\right)\right),\end{aligned} \tag{2.32}$$

$$0=\frac{\partial f(x,t)}{\partial x}, \qquad x=0, \tag{2.33}$$

$$\begin{aligned}0=f(x,t)+\frac{1}{2q(x,t)}\frac{\partial f(x,t)}{\partial x}+\frac{1}{4q(x,t)}\Bigg\{\frac{1}{q(x,t)}\frac{\partial a\left(\boldsymbol{\mathcal{C}}(x,t)\right)}{\partial x}\frac{\partial k\left(\boldsymbol{\mathcal{C}}(x,t)\right)}{\partial x}\\ +k\left(\boldsymbol{\mathcal{C}}(x,t)\right)\frac{\partial}{\partial x}\left(\frac{1}{q(x,t)}\frac{\partial a\left(\boldsymbol{\mathcal{C}}(x,t)\right)}{\partial x}\right)\\ +a\left(\boldsymbol{\mathcal{C}}(x,t)\right)\frac{\partial}{\partial x}\left(\frac{1}{q(x,t)}\frac{\partial k\left(\boldsymbol{\mathcal{C}}(x,t)\right)}{\partial x}\right)\Bigg\}, \qquad x=L(t),\end{aligned} \tag{2.34}$$

$$u(x,t)=\frac{1}{\eta q(x,t)}\frac{\partial f(x,t)}{\partial x}, \qquad x\in\left(0,L\left(t\right)\right), \tag{2.35}$$

where

$$f\left(x,t\right)=k\left(\boldsymbol{\mathcal{C}}\right)\left(\frac{1}{q(x,t)}-a\left(\boldsymbol{\mathcal{C}}\right)\right), \qquad x\in\left(0,L\left(t\right)\right), \tag{2.36}$$

and $\partial\mathcal{C}_j/\partial x=0$ at $x=0$ and $x=L(t)$.

Equations (2.31)–(2.36) are solved numerically using a boundary fixing transformation [82]. In doing so, Equations (2.31)–(2.36) are transformed from an evolving domain, $x\in[0,L(t)]$, to a fixed domain, $\xi\in[0,1]$, by setting $\xi=x/L(t)$ [82]. The transformed equations are discretised using a standard implicit finite difference method with initial conditions $q(x,0)$ and $\mathcal{C}_j(x,0)$. The numerical method is outlined in Chapter 3.2.2, and key numerical algorithms to solve the continuum model are available on GitHub.

2.3 Results

To examine the accuracy of the new free boundary model, we compare solutions from the discrete and continuum models for epithelial tissues consisting of $m = 1$ and $m = 2$ chemical species.

2.3.1 Preliminary results: Homogeneous tissue

In all simulations, an epithelial tissue with just $N = 20$ cells is considered. Choosing a relatively small value of N is a challenging scenario for the continuum model. Baker et al. [30] show that the accuracy of the continuum model increases as N increases. Additional simulations in this study with $N > 20$ confirm this (results not shown). In the discrete model, each cell i is initially the same length, $l_i(0) = 0.5$, such that $L(0) = 10$. The discrete cell density is $q_i(t) = 1/l_i(t)$ which corresponds to $q(x, 0) = 2$ for $x \in [0, L(t)]$ in the continuum model.

The simplest application of the free boundary model is to consider cell populations without mechanobiological coupling. For a homogeneous tissue with one chemical species $\boldsymbol{\mathcal{C}}(x,t) = \mathcal{C}_1(x,t)$, the cell stiffness and cell resting length are constant and independent of $\mathcal{C}_1(x,t)$. Thus, the governing equations for $q(x,t)$ and $\mathcal{C}_1(x,t)$ are only coupled through the cell velocity, $u(x,t)$. To investigate how non-uniform tissue evolution affects the chemical concentration of cells, we set $\mathcal{C}_1(x,0) = 1$ for $x \in [0, L(t)]$ and $Z_1(\mathcal{C}_1) = 0$.

Figure 2.2(a) demonstrates a rapid decrease in the cell density at $x = L(t)$ as the tissue relaxes and the cells elongate. This decreases the chemical concentration (Figure 2.2(b)). As the tissue mechanically relaxes, the cell boundaries form a non-uniform spatial discretisation on which $\mathcal{C}_1(x,t)$ is transported (Figure 2.2(a)–(b)). Figure 2.2(c)–(d) demonstrates that the continuum model accurately reflects the biological mechanisms included in the discrete model, despite the use of truncated Taylor series expansions. Additional results in Chapter 3.3 show that $q(x,t), \mathcal{C}_1(x,t)$ and $L(t)$ become constant as $t \to \infty$.

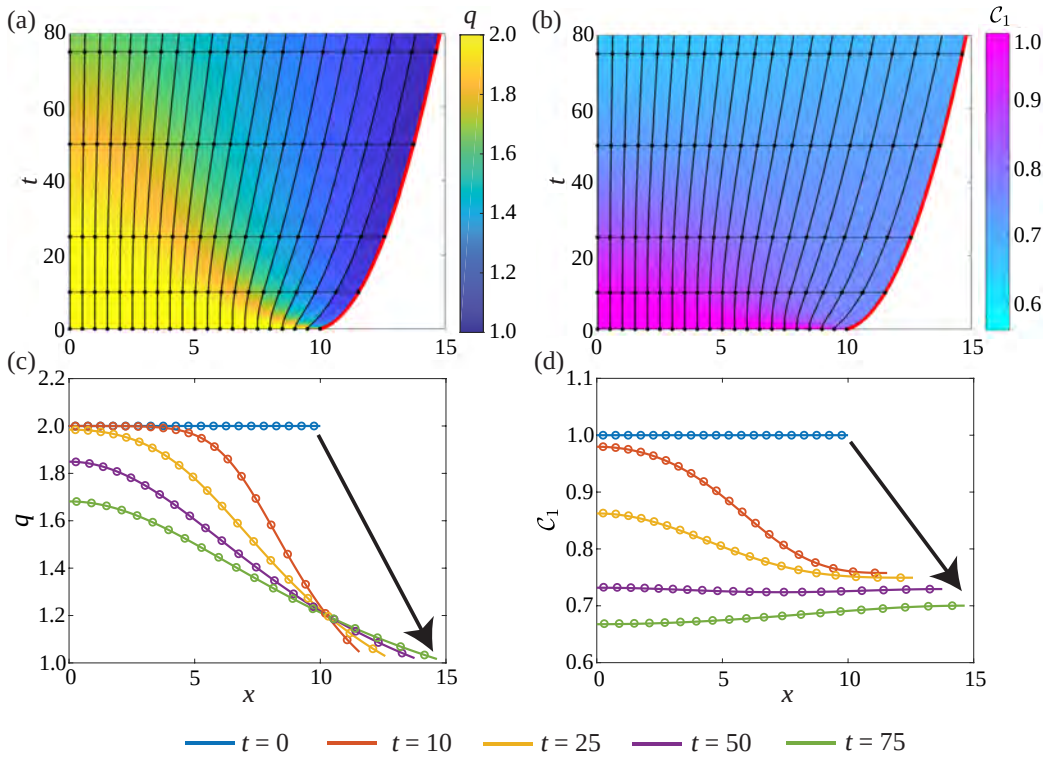

Figure 2.2: Homogeneous tissue with $N = 20$ cells and one chemical species where $Z_1(\mathcal{C}_1) = 0$, and $a = k = D_1 = \eta = 1$. Characteristic diagrams in (a)–(b) illustrate the position of cell boundaries where the free boundary is highlighted in red. The colour in (a)–(b) represents $q(x,t)$ and $\mathcal{C}_1(x,t)$ respectively. In (a)–(b), the black horizontal lines indicate times at which $q(x,t)$ and $\mathcal{C}_1(x,t)$ snapshots are shown in (c)–(d). In (c)–(d), the discrete and continuum solutions are compared as the dots and solid line respectively for $t = 0, 10, 25, 50, 75$ where the arrow represents the direction of time.

2.3.2 Case study 1: Rac–Rho pathway

We now apply the mechanobiological model to investigate the Rac–Rho pathway. Rho GTPases are a family of signalling molecules that consist of two key members, RhoA and Rac1. Rho GTPases cycle between an active and inactive state, and regulate cell size and cell motility [42, 60, 66, 68, 83]. Additionally, Rho GTPases play roles in wound healing [84] and cancer development [85, 86]. New experimental methods [87, 88] have discovered a connection between cellular mechanical tension and Rho GTPase activity [89]. Previous studies use a discrete modelling framework to investigate this relationship, and conclude that epithelial tissue dynamics is dictated by the strength of the mechanobiological coupling [60, 64]. We extend these previous results by considering how mechanobiological coupling, and

chemical variation associated with changes in cell length and diffusion, lead to oscillatory and non-oscillatory tissue dynamics.

To investigate the impact of mechanobiological coupling on epithelial tissue dynamics, we let $\boldsymbol{\mathcal{C}}(x,t) = \{\mathcal{C}_1(x,t), \mathcal{C}_2(x,t)\}$ such that $\mathcal{C}_1(x,t)$ is the concentration of RhoA and $\mathcal{C}_2(x,t)$ is the concentration of Rac1. In the discrete and continuum models, cells are assumed to behave like linear springs [31, 61]. Thus, cellular mechanical tension is defined as the difference between the length and resting length of cells. Mechanobiological coupling is proportional to cellular tension, and is included in $Z_j\left(\boldsymbol{\mathcal{C}}\right)$. As Rho GTPase activity increases cell stiffness [90], we choose $k\left(\boldsymbol{\mathcal{C}}\right)$ as an increasing function of either $\mathcal{C}_1(x,t)$ or $\mathcal{C}_2(x,t)$. Furthermore, $a\left(\boldsymbol{\mathcal{C}}\right)$ is chosen to reflect the fact that RhoA promotes cell contraction [60, 64].

The effect of RhoA is considered first, where $\boldsymbol{\mathcal{C}}(x,t) = \{\mathcal{C}_1(x,t)\}$. We include the same mechanobiological coupling as [60, 64] and let,

$$Z_1\left(\boldsymbol{\mathcal{C}}\right) = \overbrace{\left(b + \underbrace{\gamma \frac{\mathcal{C}_1^n}{1+\mathcal{C}_1^n}}_{\text{feedback loop}} + \underbrace{\beta\left(\frac{1}{q} - a\left(\mathcal{C}_1\right)\right)}_{\substack{\text{mechanobiological} \\ \text{coupling}}}\right)\left(G_{\mathrm{T}} - \mathcal{C}_1\right)}^{\text{activation}} \underbrace{- \delta \mathcal{C}_1}_{\text{deactivation}}, \tag{2.37}$$

where b is the basal activation rate, G_{T} is the total amount of active and inactive RhoA, and δ is the deactivation rate [60, 64]. The activation term contains a positive feedback loop, governed by γ, to reflect the fact that RhoA self–activates [60,64]. Mechanobiological coupling is governed by β, and is proportional to mechanical tension.

Similar to [60], we find that the tissue either mechanically relaxes or continuously oscillates depending on the choice of β (Figure 2.3). Figure 2.3(a),(c) illustrates non-oscillatory tissue behaviour when the mechanobiological coupling is weak, $\beta = 0.2$. By increasing the strength of the mechanobiological coupling to $\beta = 0.3$, we observe temporal oscillations in the tissue length and sharp transitions between high and low levels of RhoA (Figure 2.3(b),(d)). Figure 2.3(e)–(h) illustrates that the continuum model and the free boundary condition accurately describe non-oscillatory and oscillatory tissue dynamics.

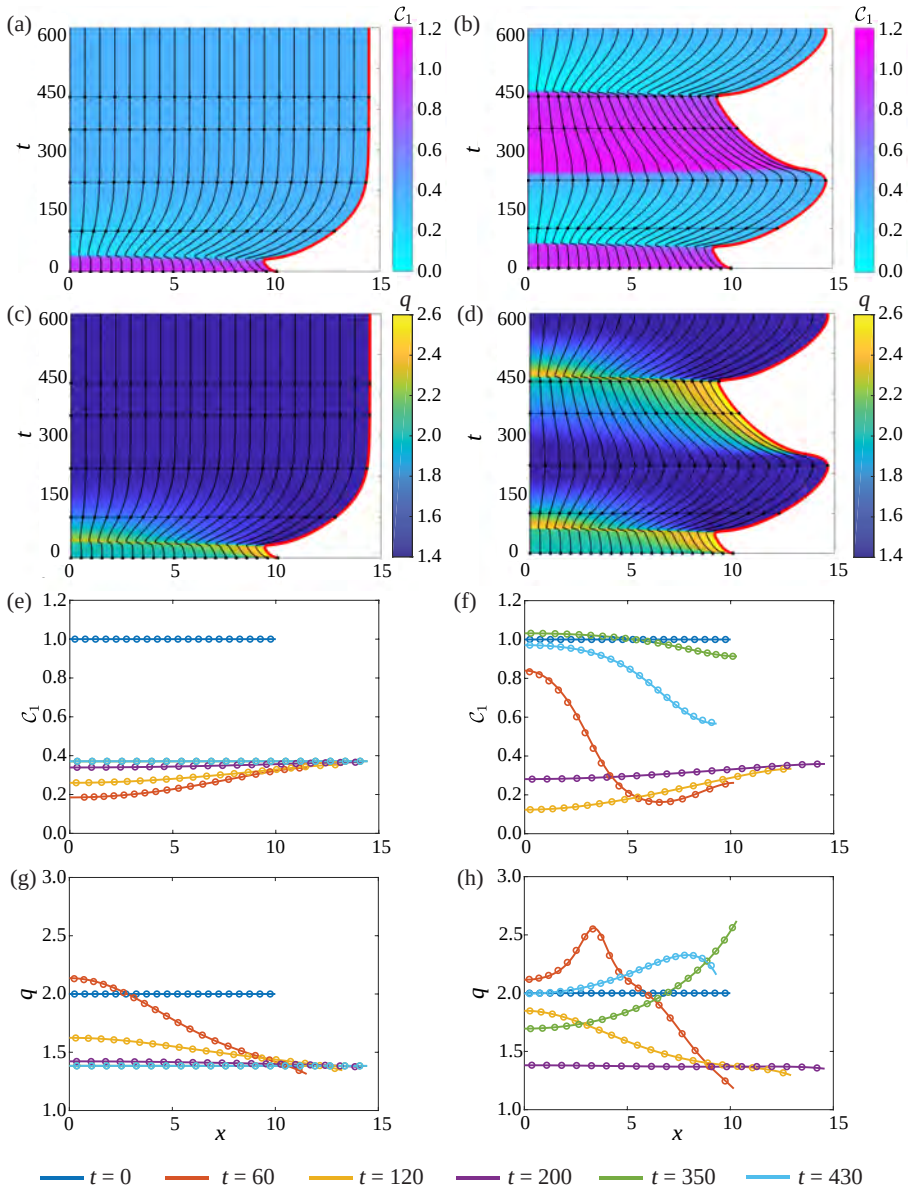

Figure 2.3: 1D tissue dynamics where RhoA is coupled to mechanical cell tension. (a),(c),(e),(g) correspond to a non-oscillatory system where $\beta = 0.2$ and (b),(d),(f),(h) relate to an oscillatory system where $\beta = 0.3$. Characteristic diagrams in (a)–(d) illustrate the evolution of cell boundaries where the free boundary is highlighted in red. The colour in (a)–(b) represents $\mathcal{C}_1(x,t)$ and $q(x,t)$ in (c)–(d). The black horizontal lines indicate times at which $\mathcal{C}_1(x,t)$ and $q(x,t)$ snapshots are shown in (e)–(f) and (g)–(h) respectively. In (e)–(h), the discrete and continuum solutions are compared as the dots and solid line respectively for $t = 0, 100, 220, 350, 430$. In both systems, $a = l_0 - \phi\mathcal{C}_1^p / \left(G_{\mathrm{h}}^p + \mathcal{C}_1^p\right)$, $k = 1 + 0.05\mathcal{C}_1$, $D_1 = 1$, $\eta = 1$, and $\mathcal{C}_1(0,t) = 1$ for $x \in [0, L(t)]$. Parameters: $b = 0.2$, $\gamma = 1.5$, $n = 4$, $p = 4$, $G_{\mathrm{T}} = 2$, $l_0 = 1$, $\phi = 0.65$, $G_{\mathrm{h}} = 0.4$, $\delta = 1$.

As diffusion is usually considered a stabilising process [1], we hypothesise that increasing D_1 could smooth the oscillations that arise when $\beta = 0.3$. Figure 2.4 illustrates that as D_1 increases, a temporal phase shift arises, but the amplitude of the oscillations remains constant. While this phase shift is not significant for a weakly coupled system (Figure 2.4(a)), it is significant for a strongly coupled system (Figure 2.4(b)). Thus, diffusion does not significantly dampen the oscillations. This test case provides further evidence of the ability of the new continuum model and free boundary condition to capture key biological mechanisms included in the discrete model (Figure 2.4).

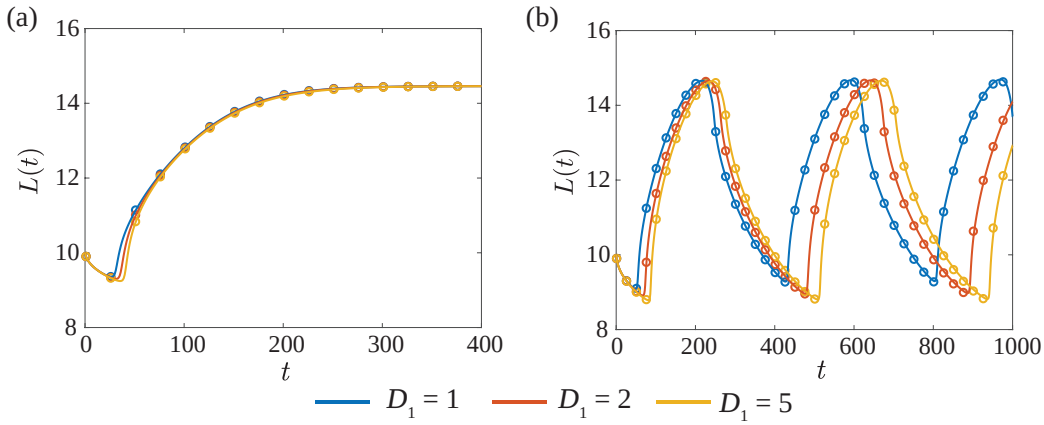

Figure 2.4: The effect of diffusion on the dynamics of the free boundary for (a) a non-oscillatory system with $\beta = 0.2$ and (b) a oscillatory system with $\beta = 0.3$. The discrete solution is shown as the dots and the continuum solution as solid line. Parameters are as in Figure 2.3.

To examine the combined effect of RhoA and Rac1 on epithelial tissue dynamics, we let $\boldsymbol{\mathcal{C}}(x,t) = \{\mathcal{C}_1(x,t), \mathcal{C}_2(x,t)\}$ and consider [60],

$$Z_1(\boldsymbol{\mathcal{C}}) = \overbrace{\left(b_1 + \underbrace{\hat{\beta}\left(\frac{1}{q} - a(\mathcal{C}_1)\right)}_{\text{mechanobiological coupling}}\right)\frac{1}{1+\mathcal{C}_2^n}(G_{1_T} - \mathcal{C}_1)}^{\text{activation}} - \underbrace{\delta_1 \mathcal{C}_1}_{\text{deactivation}}, \tag{2.38}$$

$$Z_2(\boldsymbol{\mathcal{C}}) = \underbrace{\frac{b_2}{1+\mathcal{C}_1^n}(G_{2_T} - \mathcal{C}_2)}_{\text{activation}} - \underbrace{\delta_2 \mathcal{C}_2}_{\text{deactivation}}, \tag{2.39}$$

where $\mathcal{C}_1(x,t)$ is the concentration of RhoA and $\mathcal{C}_2(x,t)$ is the concentration of Rac1. In a weakly coupled system when $\hat{\beta} = 1$, we observe the fast transition from the initial concentrations of RhoA and Rac1 to the steady state concentration

(Figure 2.5(a),(c)). Analogous to Figure 2.3(a),(c), temporal oscillations arise when the mechanobiological coupling is strong, $\hat{\beta} = 2.5$ (Figure 2.5(b),(d)).

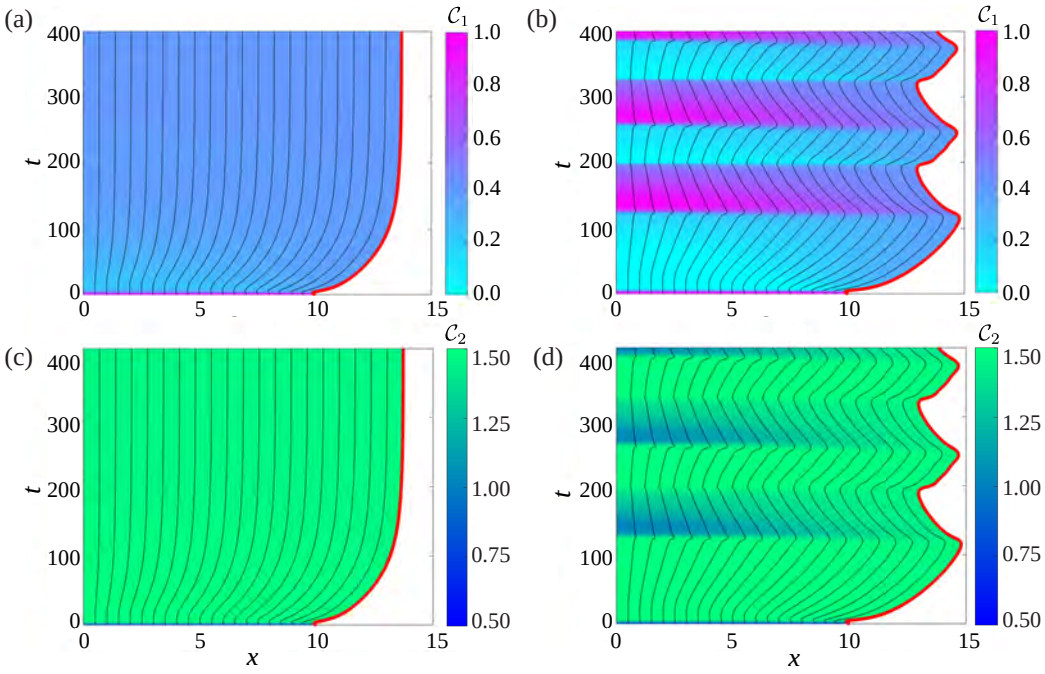

Figure 2.5: Characteristic diagrams for the interaction of RhoA and Rac1 where the free boundary is highlighted in red. (a),(c) correspond to a non-oscillatory system where $\hat{\beta} = 1$ and (b),(d) relate to an oscillatory system where $\hat{\beta} = 2.5$. The colour in (a)–(b) denotes the concentration of RhoA and the concentration of Rac1 in (c)–(d). In both systems, $a = l_0 - \phi \mathcal{C}_1^p / \left(G_{\mathrm{h}}^p + \mathcal{C}_1^p\right)$, $k = 1 + 0.1\mathcal{C}_2$, $D_1 = D_2 = 1$ and $\eta = 1$. The initial conditions are $\mathcal{C}_1(0,t) = 1$ and $\mathcal{C}_2(0,t) = 0.5$ for $x \in [0, L(t)]$. Parameters: $b_1 = b_2 = 1$, $\delta_1 = \delta_2 = 1$, $n = 3$, $p = 4$, $G_{1_{\mathrm{T}}} = 2$, $G_{2_{\mathrm{T}}} = 3$, $l_0 = 1$, $\phi = 0.65$, $G_{\mathrm{h}} = 0.4$. Discrete and continuum solutions are compared in Chapter 3.4.

The mechanobiological coupling and intracellular signalling in Figures 2.3–2.5 extend upon previous Rho GTPase models [60, 64]. The source terms stated in Equations (2.37)–(2.39) can be applied to a single, spatially–uniform cell to determine the dependence of the system stability on model parameters [60]. This analysis is outlined in Chapter 3.4.1 and was used to inform our choices of β and $\hat{\beta}$.

2.3.3 Case study 2: Activator–inhibitor patterning

Case study 2 considers an activator–inhibitor system [1, 91, 92]. Previous studies of activator–inhibitor patterns on uniformly evolving domains have characterised the pattern splitting and frequency doubling phenomena which occur naturally on the skin of angelfish [51, 52, 72–74]. To investigate how diffusion driven instabilities arise on a non-uniformly evolving domain, we let $\boldsymbol{\mathcal{C}}(x,t) = \{\mathcal{C}_1(x,t), \mathcal{C}_2(x,t)\}$ with $D_1 \neq D_2$, and use Schnakenberg kinetics,

$$Z_1\left(\boldsymbol{\mathcal{C}}\right) = n_1 - n_2\mathcal{C}_1 + n_3\mathcal{C}_1^2\mathcal{C}_2, \tag{2.40}$$

$$Z_2\left(\boldsymbol{\mathcal{C}}\right) = n_4 - n_3\mathcal{C}_1^2\mathcal{C}_2, \tag{2.41}$$

where $\mathcal{C}_1(x,t)$ is the activator and $\mathcal{C}_2(x,t)$ is the inhibitor [1]. The parameters, $n_i > 0$ for $i = 1, 2, 3, 4$, govern activator–inhibitor interactions. Non-dimensionalisation of the governing equations (Equations (2.25) and (2.29)) reveals that the linear stability analysis is analogous to the classical stability analysis of Turing patterns on fixed domains [1]. Thus, we define the relative diffusivity, $d = D_2/D_1$, with the expectation that there exists a critical value, d_c, that depends upon the choice of n_i. In doing so, it is expected that diffusion driven instabilities arise for $d > d_c$ [1, 91].

A homogeneous tissue is initialised to investigate the affect of d on the evolution of activator–inhibitor patterns. For $d < d_c$, the distribution of $\mathcal{C}_1(x,t)$ and $\mathcal{C}_2(x,t)$ varies in time but remains approximately spatially uniform throughout the tissue (Figure 2.6(a),(c),(e),(g)). Thus, only temporal patterning arises when $d < d_c$. Figure 2.6(b),(d),(f),(h) demonstrates that spatial–temporal patterns develop when $d > d_c$. Similar to [51, 52, 73], we observe splitting in activator peaks for $d > d_c$ where the concentration of $\mathcal{C}_1(x,t)$ is at a minimum. Figure 2.6(b) shows that two distinct activator peaks arise. The long time behaviour of the tissue is examined in Chapter 3.5. Figure 2.6(e),(g) shows excellent agreement between the solutions of the discrete and continuum models when $d < d_c$, whereas Figure 2.6(f),(h) shows a small discrepancy between the solutions of the discrete and continuum models when $d > d_c$.

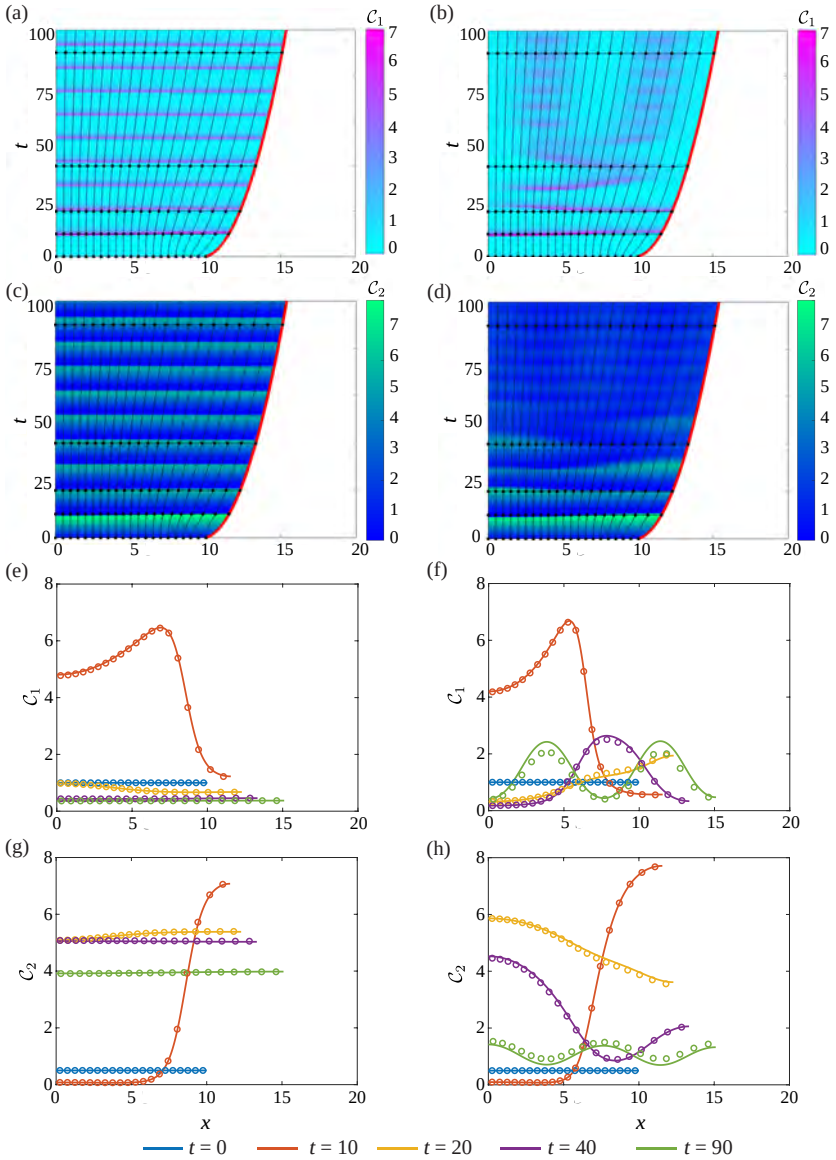

Figure 2.6: The evolution of activator–inhibitor patterns in a homogeneous tissue with Schnakenberg dynamics. In (a),(c),(e),(g), $D_1 = 2$ and $D_2 = 3$ such that $d < d_c$. In (b),(d),(f),(h), $D_1 = 0.5$ and $D_2 = 5$ such that $d > d_c$. Characteristic diagrams in (a)–(d) illustrate the evolution of cell boundaries where the free boundary is highlighted in red. The colour in (a)–(b) represents $\mathcal{C}_1(x,t)$ and $\mathcal{C}_2(x,t)$ in (c)–(d). The black horizontal lines indicate times at which $\mathcal{C}_1(x,t)$ and $\mathcal{C}_2(x,t)$ snapshots are shown in (e)–(f) and (g)–(h) respectively. In (e)–(h), the discrete and continuum solutions are compared as the dots and solid line respectively for $t = 0, 10, 20, 40, 90$. In both systems, $\mathcal{C}_1(x,0) = 1$ and $\mathcal{C}_2(x,0) = 0.5$ for $x \in [0, L(t)]$ and $a = k = \eta = 1$ Parameters: $n_1 = 0.1, n_2 = 1, n_3 = 0.5, n_4 = 1$ and $d_c = 4.9842$

2.4 Conclusion

In this study, we present a novel free boundary mechanobiological model to describe epithelial tissue dynamics. A discrete modelling framework is used to include mechanobiological coupling at the cell level. Tissue–level outcomes are described by a system of coupled, non-linear partial differential equations, where the evolution of the free boundary is governed by a novel boundary condition. In contrast to previous free boundary models, the elongation of the tissue is not pre-specified [48–52, 73, 74], or described by a classical one–phase Stefan condition [53, 54]. We take the continuum limit description of the discrete model to derive a novel free boundary condition which describes how mechanobiological coupling dictates epithelial tissue dynamics. In deriving the continuum model, we make reasonable assumptions that N is sufficiently large, and that the time scale of mechanical relaxation is sufficiently fast (mechanical relaxation is much faster than cell proliferation [38]). Case studies involving a homogeneous cell population, the Rac–Rho pathway and activator–inhibitor patterning demonstrate that the continuum model reflects the biologically–motivated discrete model even when N is relatively small. These case studies show how non-uniform tissue dynamics, including oscillatory and non-oscillatory tissue behaviour, arises due to mechanobiological coupling.

There are several possible mathematical and biological extensions of this study. We take the most fundamental approach and choose a linear force law to describe cell-to-cell interactions. One extension of this work is to describe cell-to-cell interactions using a non-linear force law, provided there is some justification that the linear force law is inadequate [30, 61]. Another choice we make is to suppose that chemical transport is described by linear diffusion at the macroscopic scale. Other choices, such as diffusion with drift, are possible [93]. Another extension of the free boundary model is to introduce cell proliferation and cell death [30, 38, 94]. While these phenomena traditionally depend on cell length [30, 38], the general theoretical framework presented here is compatible with cell proliferation and death that depend on intracellular signalling. In doing so, the model is applicable to biochemical networks where biological mechanisms regulate cell proliferation in epithelial tissues [95].

Chapter 3

Mathematical techniques for a free boundary mechanobiological model of epithelial tissues

This chapter comprises of the supplementary material of a preprint available on bioRxiv. This preprint is under review at *Proceedings of the Royal Society A: Mathematical, Physical and Engineering Sciences* as:

A free boundary mechanobiological model of epithelial tissues

Tamara A. Tambyah, Ryan J. Murphy, Pascal R. Buenzli and Matthew J. Simpson

3.1 Continuum model derivation

3.1.1 Change of variables

This section outlines the change of variables from $(\bar{i}, t)$ to (x, t) used in Chapter 2.2.2. Rewriting Equation (2.11), the cell density per unit length, $q(x,t)$, is

$$q(x,t) = N\frac{\partial \bar{i}(x,t)}{\partial x}. \tag{3.1}$$

To perform a change of variables from $(\bar{i}, t)$ to (x, t), we calculate the Jacobian of the coordinate transformation [30, 31, 61],

$$\begin{pmatrix} \frac{\partial x}{\partial \bar{i}}\big|_t & \frac{\partial x}{\partial t}\big|_{\bar{i}} \\ \frac{\partial t}{\partial \bar{i}}\big|_t & \frac{\partial t}{\partial t}\big|_{\bar{i}} \end{pmatrix} = \begin{pmatrix} \frac{\partial \bar{i}}{\partial x}\Big|_t & \frac{\partial \bar{i}}{\partial t}\Big|_x \\ \frac{\partial t}{\partial x}\big|_t & \frac{\partial t}{\partial t}\big|_x \end{pmatrix}^{-1}, \tag{3.2}$$

$$= \frac{1}{\frac{\partial \bar{i}}{\partial x}\Big|_t \frac{\partial t}{\partial t}\big|_x - \frac{\partial \bar{i}}{\partial t}\Big|_x \frac{\partial t}{\partial x}\big|_t} \begin{pmatrix} \frac{\partial t}{\partial t}\big|_x & -\frac{\partial \bar{i}}{\partial t}\Big|_x \\ -\frac{\partial t}{\partial x}\big|_t & \frac{\partial \bar{i}}{\partial x}\Big|_t \end{pmatrix}, \tag{3.3}$$

to arrive at the relationships,

$$\frac{\partial x}{\partial \bar{i}} = \frac{N}{q}, \qquad \frac{\partial x}{\partial t} = -\frac{N}{q}\frac{\partial \bar{i}}{\partial t}. \tag{3.4}$$

Using the chain rule, the second derivatives are,

$$\frac{\partial^2 x}{\partial \bar{i}^2} = \frac{\partial x}{\partial \bar{i}}\frac{\partial}{\partial x}\left(\frac{N}{q}\right) = -\frac{N^2}{q^3}\frac{\partial q}{\partial x}, \tag{3.5}$$

$$\frac{\partial^2 k}{\partial \bar{i}^2} = \frac{\partial x}{\partial \bar{i}}\frac{\partial}{\partial x}\left(\frac{\partial k}{\partial x}\frac{\partial x}{\partial \bar{i}}\right) = \frac{N^2}{q}\frac{\partial}{\partial x}\left(\frac{1}{q}\frac{\partial k}{\partial x}\right), \tag{3.6}$$

$$\frac{\partial^2 a}{\partial \bar{i}^2} = \frac{\partial x}{\partial \bar{i}}\frac{\partial}{\partial x}\left(\frac{\partial a}{\partial x}\frac{\partial x}{\partial \bar{i}}\right) = \frac{N^2}{q}\frac{\partial}{\partial x}\left(\frac{1}{q}\frac{\partial a}{\partial x}\right). \tag{3.7}$$

3.1.2 Derivation of governing equation for cell density in factorised form

Here we outline how Equations (2.23), (2.25) and (2.28) can be obtained using the factorised form of $f(\bar{i}, t)$ in Equation (2.13). The equations of motion in Equations

(2.14)–(2.16) are restated as,

$$\eta\frac{\partial x(\bar{i},t)}{\partial t} = 0, \qquad \bar{i} = 0, \tag{3.8}$$

$$\eta\frac{\partial x(\bar{i},t)}{\partial t} = f\left(\bar{i}+1/N,t\right) - f\left(\bar{i},t\right), \qquad \bar{i} \in (1/N,1), \tag{3.9}$$

$$\eta\frac{\partial x(\bar{i},t)}{\partial t} = -f\left(\bar{i},t\right), \qquad \bar{i} = 1. \tag{3.10}$$

To derive the local cell velocity in Equation (2.23), the right hand side of Equation (3.9) is expanded in a Taylor series about $\bar{i}$,

$$\eta\frac{\partial x}{\partial t} = \frac{1}{N}\frac{\partial f}{\partial \bar{i}} + \mathcal{O}\left(N^{-2}\right), \qquad \bar{i} \in (1/N,1). \tag{3.11}$$

Neglecting non-zero higher order terms and using the chain rule gives,

$$\eta\frac{\partial x}{\partial t} = \frac{1}{N}\frac{\partial f}{\partial x}\frac{\partial x}{\partial \bar{i}}, \qquad \bar{i} \in (1/N,1). \tag{3.12}$$

Equation (3.4) is substituted into the right hand side of Equation (3.12) to derive the local cell velocity, $u(x,t) = \partial x/\partial t$, as,

$$u(x,t) = \frac{1}{\eta q(x,t)}\frac{\partial f(x,t)}{\partial x}, \qquad x \in \left(0, L\left(t\right)\right). \tag{3.13}$$

As $u(x,t) = \partial x/\partial t$, Equation (3.4) is substituted into the left hand side of Equation (3.13). Differentiating the resulting equation with respect to x gives,

$$\frac{\partial}{\partial x}\left(N\frac{\partial \bar{i}}{\partial t}\right) = \frac{\partial}{\partial x}\left(-\frac{1}{\eta}\frac{\partial f(x,t)}{\partial x}\right), \qquad x \in \left(0, L\left(t\right)\right). \tag{3.14}$$

The order of differentiation on the left hand side of Equation (3.14) is reversed, and Equation (3.4) is used to give,

$$\frac{\partial q(x,t)}{\partial t} = -\frac{1}{\eta}\frac{\partial^2 f(x,t)}{\partial x^2}, \qquad x \in \left(0, L\left(t\right)\right). \tag{3.15}$$

To derive the left boundary condition in Equation (2.28), the left hand side of Equation (3.8) is equated to Equation (3.13) giving,

$$\frac{\partial f(x,t)}{\partial x} = 0, \qquad x = 0. \tag{3.16}$$

Thus, we have shown that Equations (2.23), (2.25) and (2.28) can be obtained using the factorised form of $f\left(\bar{i},t\right)$ in Equation (2.13), and first order Taylor se-

ries expansions. In the main document we do not pursue this approach. This is because more care is required to obtain the correct form of the free boundary equation in Equation (2.27). Extensive numerical exploration confirms that the approach taken in the main document is necessary to reflect the underlying biological mechanisms included in the discrete model.

3.2 Numerical methods

This section outlines the numerical method used to solve the discrete and continuum models with one chemical species, $m = 1$. Key numerical algorithms for $m = 1$ and $m = 2$ chemical species are available on GitHub.

3.2.1 Discrete model

For N cells and one chemical species, the discrete model consists of $2N+1$ ordinary differential equations. For simplicity, we write $\mathbf{C} = C^{(1)} = C$ and $D_1 = D$. Equations (2.1)–(2.10) are restated as:

$$\eta\frac{\mathrm{d}x_0}{\mathrm{d}t} = 0, \tag{3.17}$$

$$\eta\frac{\mathrm{d}x_i}{\mathrm{d}t} = f_{i+1} - f_i, \qquad i = 1, \ldots, N-1, \tag{3.18}$$

$$\eta\frac{\mathrm{d}x_N}{\mathrm{d}t} = -f_N, \tag{3.19}$$

$$\frac{\mathrm{d}C_1}{\mathrm{d}t} = Z\left(C_1\right) - \frac{C_1}{l_1}\frac{\mathrm{d}l_1}{\mathrm{d}t} + \frac{1}{l_1}\left(T_2^- C_2 l_2 - T_1^+ C_1 l_1\right), \tag{3.20}$$

$$\begin{aligned}\frac{\mathrm{d}C_i}{\mathrm{d}t} &= Z\left(C_i\right) - \frac{C_i}{l_i}\frac{\mathrm{d}l_i}{\mathrm{d}t} \\ &+ \frac{1}{l_i}\left(T_{i-1}^+ C_{i-1} l_{i-1} - \left(T_i^+ + T_i^-\right) C_i l_i + T_{i+1}^- C_{i+1} l_{i+1}\right), \quad i = 1, \ldots, N-1,\end{aligned} \tag{3.21}$$

$$\frac{\mathrm{d}C_N}{\mathrm{d}t} = Z\left(C_N\right) - \frac{C_N}{l_N}\frac{\mathrm{d}l_N}{\mathrm{d}t} + \frac{1}{l_N}\left(T_{N-1}^+ C_{N-1} l_{N-1} - T_N^- C_N l_N\right), \tag{3.22}$$

where $l_i = x_i(t) - x_{i-1}(t)$ is the length of cell i and

$$f_i = k\left(C_i\right)\left(x_i(t) - x_{i-1}(t) - a\left(C_i\right)\right), \qquad i = 1, \ldots, N. \tag{3.23}$$

The transport rates for internal cells are

$$T_i^- = \frac{2D}{\left(y_i(t) - y_{i-1}(t)\right)\left(y_{i+1}(t) - y_{i-1}(t)\right)}, \qquad i = 2, \ldots, N-1, \tag{3.24}$$

$$T_i^+ = \frac{2D}{\left(y_{i+1}(t) - y_i(t)\right)\left(y_{i+1}(t) - y_{i-1}(t)\right)}, \qquad i = 2, \ldots, N-1, \tag{3.25}$$

and

$$T_1^+ = \frac{2D}{(y_2(t) - y_1(t))\,(y_2(t) + y_1(t))}, \tag{3.26}$$

$$T_N^- = \frac{2D}{(y_N(t) - y_{N-1}(t))\,(x_N(t) - y_N(t) - y_{N-1}(t))}, \tag{3.27}$$

and $T_1^- = T_N^+ = 0$ for boundary cells [80]. Equations (3.17)–(3.27) are solved numerically using `ode15s` in MATLAB [81]. At each time step, we use a Voronoi partition to compute the resident points, $y_i(t)$, and the transport rates, $T_i^{\pm}$.

Voronoi partition

To define a Voronoi partition, we set the resident point of cell 1, $y_1(t)$, as the midpoint of its respective cell boundaries,

$$y_1(t) = \frac{x_0(t) + x_1(t)}{2}. \tag{3.28}$$

The Voronoi partition enforces that the cell boundaries correspond to the midpoints of resident points [80]. Thus, the following relationship holds

$$x_{i-1}(t) = \frac{y_i(t) + y_{i-1}(t)}{2}, \qquad i = 2, \ldots, N. \tag{3.29}$$

Equations (3.28) and (3.29) can be written as the following system of linear equations,

$$\begin{bmatrix} 1 & 0 & 0 & 0 & 0 \\ 1 & 1 & 0 & 0 & 0 \\ 0 & 1 & 1 & 0 & 0 \\ \vdots & \ddots & \ddots & \ddots & \ddots \\ 0 & 0 & 0 & 1 & 1 \end{bmatrix} \begin{bmatrix} y_1(t) \\ y_2(t) \\ y_3(t) \\ \vdots \\ y_N(t) \end{bmatrix} = \begin{bmatrix} (x_0(t) + x_1(t))/2 \\ 2x_1(t) \\ 2x_2(t) \\ \vdots \\ 2x_{N-1}(t) \end{bmatrix}. \tag{3.30}$$

Equation (3.30) is solved numerically for the resident points at each time step of the discrete simulation. As Equation (3.30) is a lower triangular matrix system, we use the Thomas Algorithm [96].

3.2.2 Continuum model

We now outline the numerical method used to solve the continuum model and write $\boldsymbol{\mathcal{C}} = \mathcal{C}_1 = \mathcal{C}$ and $D_1 = D$ for simplicity. Equations (2.31)–(2.36) are restated

as a system of coupled, non-linear partial differential equations:

$$\frac{\partial q}{\partial t} = -\frac{1}{\eta}\frac{\partial^2 f}{\partial x^2}, \qquad x \in (0, L(t)), \tag{3.31}$$

$$\frac{\partial \mathcal{C}}{\partial t} + \frac{\partial}{\partial x}\left(u\mathcal{C} - D\frac{\partial \mathcal{C}}{\partial x}\right) = Z(\mathcal{C}), \qquad x \in (0, L(t)), \tag{3.32}$$

$$0 = \frac{\partial f}{\partial x}, \qquad x = 0, \tag{3.33}$$

$$0 = f + \frac{1}{2q}\frac{\partial f}{\partial x} + \frac{1}{4q}\left\{\frac{1}{q}\frac{\partial a}{\partial x}\frac{\partial k}{\partial x} + k\frac{\partial}{\partial x}\left(\frac{1}{q}\frac{\partial a}{\partial x}\right) + a\frac{\partial}{\partial x}\left(\frac{1}{q}\frac{\partial k}{\partial x}\right)\right\}, \qquad x = L(t), \tag{3.34}$$

$$u = \frac{1}{\eta q}\frac{\partial f}{\partial x}, \qquad x \in (0, L(t)), \tag{3.35}$$

where

$$f = k\left(\frac{1}{q} - a\right), \qquad x \in (0, L(t)), \tag{3.36}$$

and $\partial \mathcal{C}/\partial x = 0$ at $x = 0$ and $x = L(t)$.

A standard boundary fixing transformation is used to transform Equations (3.31)–(3.36) from an evolving domain, $x \in [0, L(t)]$, to a fixed domain, $\xi \in [0, 1]$, by setting $\xi = x/L(t)$ [82]. Invoking this transform yields:

$$\frac{\partial q}{\partial t} = -\frac{1}{\eta L^2}\frac{\partial^2 f}{\partial \xi^2} + \frac{\xi}{L}\frac{\mathrm{d}L}{\mathrm{d}t}\frac{\partial q}{\partial \xi}, \qquad \xi \in (0, 1), \tag{3.37}$$

$$\frac{\partial \mathcal{C}}{\partial t} + v\frac{\partial \mathcal{C}}{\partial \xi} + \frac{\mathcal{C}}{\eta q L^2}\left\{\frac{\partial^2 f}{\partial \xi^2} - \frac{1}{q}\frac{\partial q}{\partial \xi}\frac{\partial f}{\partial \xi}\right\} - \frac{D}{L^2}\frac{\partial^2 \mathcal{C}}{\partial \xi^2} = Z(\mathcal{C}), \qquad \xi \in (0, 1), \tag{3.38}$$

$$0 = \frac{1}{L}\frac{\partial f}{\partial \xi}, \qquad \xi = 0, \tag{3.39}$$

$$0 = f + \frac{1}{2qL}\frac{\partial f}{\partial \xi} + \frac{k}{4qL^2}\frac{\partial}{\partial \xi}\left(\frac{1}{q}\frac{\partial a}{\partial \xi}\right) + \frac{1}{4q^2L^2}\frac{\partial a}{\partial \xi}\frac{\partial k}{\partial \xi} + \frac{a}{4qL^2}\frac{\partial}{\partial \xi}\left(\frac{1}{q}\frac{\partial k}{\partial \xi}\right), \qquad \xi = 1, \tag{3.40}$$

$$u = \frac{1}{\eta q L}\frac{\partial f}{\partial \xi}, \qquad \xi \in (0, 1), \tag{3.41}$$

where

$$v = \frac{1}{\eta q L^2}\frac{\partial f}{\partial \xi} - \frac{\xi}{L}\frac{\mathrm{d}L}{\mathrm{d}t}, \qquad \xi \in (0, 1), \tag{3.42}$$

and $\partial \mathcal{C}/\partial \xi = 0$ at $\xi = 0$ and $\xi = 1$.

Equations (3.37)–(3.42) are spatially discretised on a uniform mesh, with $n = 1/\Delta\xi + 1$ nodes. The value of $q(\xi, t)$ and $\mathcal{C}(\xi, t)$ at the i^{th} spatial node and the j^{th} temporal node are approximated as q_i^j and $\mathcal{C}_i^j$ respectively, where $\xi = (i-1)\Delta\xi$ and $t = j\Delta t$. A standard implicit finite difference method is used to approximate spatial and temporal derivatives [96].

We first consider the discretisation of the governing equation and boundary conditions for cell density. Central difference approximations are used to discretise Equation (3.37) as

$$\begin{aligned}\frac{q_i^{j+1} - q_i^j}{\Delta t} = &-\frac{1}{\eta (L^{j+1})^2}\left(\frac{f_{i-1}^{j+1} - 2f_i^{j+1} + f_{i+1}^{j+1}}{(\Delta\xi)^2}\right) \\ &+ \frac{\xi}{L^{j+1}}\left(\frac{L^{j+1} - L^j}{\Delta t}\right)\left(\frac{q_{i+1}^{j+1} - q_{i-1}^{j+1}}{2\Delta\xi}\right), \qquad i = 2, \ldots, n-1.\end{aligned} \tag{3.43}$$

Equations (3.39) and (3.40) are discretised using appropriate forward and backward difference approximations,

$$0 = f_2^{j+1} - f_1^{j+1}, \tag{3.44}$$

$$\begin{aligned}0 = &f_n^{j+1} + \frac{1}{2q_n^{j+1} L^{j+1}}\left(\frac{f_n^{j+1} - f_{n-1}^{j+1}}{\Delta\xi}\right) \\ &+ \frac{k_n^{j+1}}{4q_n^{j+1}(L^{j+1})^2}\left(\frac{1}{q_n^{j+1}} - \frac{1}{q_{n-1}^{j+1}}\right)\left(\frac{a_n^{j+1} - a_{n-1}^{j+1}}{\Delta\xi}\right) \\ &+ \frac{a_n^{j+1}}{4q_n^{j+1}(L^{j+1})^2}\left(\frac{1}{q_n^{j+1}} - \frac{1}{q_{n-1}^{j+1}}\right)\left(\frac{k_n^{j+1} - k_{n-1}^{j+1}}{\Delta\xi}\right) \\ &+ \frac{1}{4\left(q_i^{j+1}\right)^2 (L^{j+1})^2}\left(\frac{a_n^{j+1} - a_{n-1}^{j+1}}{\Delta\xi}\right)\left(\frac{k_n^{j+1} - k_{n-1}^{j+1}}{\Delta\xi}\right).\end{aligned} \tag{3.45}$$

We now consider the discretisation of the governing equation and boundary conditions for $\mathcal{C}$. As $\mathcal{C}$ propagates along cell boundary characteristics, Equation (3.42) is used to upwind the first derivative of $\mathcal{C}$ in Equation (3.38). For $v_i > 0$, a backward difference approximation is used to approximate the first derivative of $\mathcal{C}$, and all other spatial derivates are approximated using central difference

approximations,

$$\frac{\mathcal{C}_i^{j+1}-\mathcal{C}_i^j}{\Delta t}+v_i\left(\frac{\mathcal{C}_i^{j+1}-\mathcal{C}_{i-1}^{j+1}}{\Delta\xi}\right)-\frac{D}{\left(L^{j+1}\right)^2}\left(\frac{\mathcal{C}_{i-1}^{j+1}-2\mathcal{C}_i^{j+1}+\mathcal{C}_{i+1}^{j+1}}{\left(\Delta\xi\right)^2}\right)$$
$$+\frac{\mathcal{C}_i^{j+1}}{\eta q_i^{j+1}\left(L^{j+1}\right)^2}\left\{\left(\frac{f_{i-1}^{j+1}-2f_i^{j+1}+f_{i+1}^{j+1}}{\left(\Delta\xi\right)^2}\right)\right. \tag{3.46}$$
$$\left.-\frac{1}{q_i^{j+1}}\left(\frac{q_{i+1}^{j+1}-q_{i-1}^{j+1}}{\Delta\xi}\right)\left(\frac{f_{i+1}^{j+1}-f_{i-1}^{j+1}}{\Delta\xi}\right)\right\}=Z\left(\mathcal{C}_i^{j+1}\right),\quad i=2,\ldots,n-1,$$

where

$$v_i=\frac{1}{\eta q_i^{j+1}\left(L^{j+1}\right)^2}\left(\frac{f_{i+1}^{j+1}-f_{i-1}^{j+1}}{2\Delta\xi}\right)-\frac{\xi}{L^{j+1}}\left(\frac{L^{j+1}-L^j}{\Delta t}\right), \tag{3.47}$$
$$i=2,\ldots,n-1.$$

Similarly, forward difference approximations are used when $v_i<0$. The boundary condition at $\xi=0$ is

$$0=\mathcal{C}_2-\mathcal{C}_1. \tag{3.48}$$

Numerical exploration revealed that a ghost node was necessary to solve $\partial\mathcal{C}/\partial\xi=0$ at $\xi=1$. The use of a ghost node ensured that the numerical solution of the continuum model agreed with the solution of the discrete model. The ghost node is placed outside the right domain boundary at $i=n+1$. A central difference approximation is applied to the zero–flux boundary condition to obtain $\mathcal{C}_{n+1}^{j+1}=\mathcal{C}_{n-1}^{j+1}$. To incorporate the ghost node, Equation (3.38) is factorised as

$$\frac{\partial\mathcal{C}}{\partial t}+v\frac{\partial\mathcal{C}}{\partial\xi}+\frac{\mathcal{C}}{\eta L^2}\frac{\partial}{\partial\xi}\left(\frac{1}{q}\frac{\partial f}{\partial\xi}\right)-\frac{D}{L^2}\frac{\partial^2\mathcal{C}}{\partial\xi^2}=Z\left(\mathcal{C}\right). \tag{3.49}$$

Backward and central difference approximations are used to discretise Equation (3.49) as

$$\frac{\mathcal{C}_n^{j+1}-\mathcal{C}_n^j}{\Delta t}+v_n\left(\frac{\mathcal{C}_n^{j+1}-\mathcal{C}_{n-1}^{j+1}}{\Delta\xi}\right)-\frac{D}{\left(L^{j+1}\right)^2}\left(\frac{\mathcal{C}_{n-1}^{j+1}-2\mathcal{C}_n^{j+1}+\mathcal{C}_{n+1}^{j+1}}{\Delta\xi^2}\right)$$
$$+\frac{\mathcal{C}_n^{j+1}}{\eta\left(L^{j+1}\right)^2}\frac{1}{\Delta\xi}\left\{\frac{1}{q_n^{j+1}}\left(\frac{f_n^{j+1}-f_{n-1}^{j+1}}{\Delta\xi}\right)-\frac{1}{q_{n-1}^{j+1}}\left(\frac{f_n^{j+1}-f_{n-1}^{j+1}}{\Delta\xi}\right)\right\} \tag{3.50}$$
$$=Z\left(\mathcal{C}_n^{j+1}\right).$$

Substituting $\mathcal{C}_{n+1}^{j+1} = \mathcal{C}_{n-1}^{j+1}$ into Equation (3.50) and factorising gives

$$\begin{aligned}&\frac{\mathcal{C}_n^{j+1} - \mathcal{C}_n^j}{\Delta t} + v_n \left(\frac{\mathcal{C}_n^{j+1} - \mathcal{C}_{n-1}^{j+1}}{\Delta \xi} \right) - \frac{D}{\left(L^{j+1}\right)^2} \left(\frac{2\mathcal{C}_{n-1}^{j+1} - 2\mathcal{C}_n^{j+1}}{\left(\Delta \xi\right)^2} \right) \\ &+ \frac{\mathcal{C}_n^{j+1}}{\eta \left(L^{j+1}\right)^2} \frac{1}{\Delta \xi} \left(\frac{1}{q_n^{j+1}} - \frac{1}{q_{n-1}^{j+1}} \right) \left(\frac{f_n^{j+1} - f_{n-1}^{j+1}}{\Delta \xi} \right) = Z\left(\mathcal{C}_n^{j+1}\right),\end{aligned} \tag{3.51}$$

where

$$v_n = \frac{1}{\eta q_n^{j+1} \left(L^{j+1}\right)^2} \left(\frac{f_n^{j+1} - f_{n-1}^{j+1}}{\Delta \xi} \right) - \frac{\xi}{L^{j+1}} \left(\frac{L^{j+1} - L^j}{\Delta t} \right). \tag{3.52}$$

Equation (3.36) is discretised as

$$f_i^{j+1} = k\left(\mathcal{C}_i^{j+1}\right) \left(\frac{1}{q_i^{j+1}} - a\left(\mathcal{C}_i^{j+1}\right) \right), \qquad i = 1, \ldots, n, \tag{3.53}$$

and substituted into Equations (3.43)–(3.52) to form a non-linear system of equations.

We solve Equations (3.43)–(3.45) for q_i^{j+1} and Equations (3.46)–(3.48),(3.51)–(3.52) for $\mathcal{C}_i^{j+1}$ using the Newton-Raphson method [97]. At each Newton-Raphson iteration, Equation (3.41) is used to update the position of the free boundary as

$$L^{j+1} = L^j + \frac{\Delta t}{\eta q_n^{j+1} L^j} \frac{f_n^{j+1} - f_{n-1}^{j+1}}{\Delta \xi}. \tag{3.54}$$

Newton-Raphson iterations are continued until the norm of the difference between successive solution estimates of q_i^{j+1} and $\mathcal{C}_i^{j+1}$ are both less than a specified tolerance, ϵ. To ensure all numerical results are grid–independent, $\Delta\xi = 10^{-3}$, $\Delta t = 10^{-3}$ and $\epsilon = 10^{-8}$. All linear systems are solved using the Thomas algorithm [96].

3.3 Preliminary results: Homogeneous tissue

In Chapter 2.3.1, we examine a homogeneous tissue with $N = 20$ cells, one chemical species, $\boldsymbol{\mathcal{C}}(x,t) = \mathcal{C}_1(x,t)$, and no chemical source, $Z_1(\mathcal{C}_1) = 0$. Figure 3.1(a)–(b) demonstrates that $q(x,t)$, $\mathcal{C}_1(x,t)$ and $L(t)$ become constant as $t \to \infty$. To obtain expressions for the long time behaviour of $q(x,t)$, $\mathcal{C}_1(x,t)$ and $L(t)$, the total number of cells, N, and total number of chemical particles, P, are computed as,

$$N = \int_0^{L(t)} q(x,t)\ \mathrm{d}x, \qquad\qquad P = \int_0^{L(t)} \mathcal{C}_1(x,t)\ \mathrm{d}x. \tag{3.55}$$

Using Equation (3.55), $N = q(x,0)L(0)$ and $P = \mathcal{C}_1(x,0)L(0)$. As the tissue relaxes, the cells elongate such that the length of individual cells approaches the cell resting length. Thus, $q(x,t)$, $\mathcal{C}_1(x,t)$ and $L(t)$ become constant,

$$\lim_{t\to\infty} q(x,t) = \frac{1}{a}, \qquad \lim_{t\to\infty} \mathcal{C}_1(x,t) = \frac{P}{Na}, \qquad \lim_{t\to\infty} L(t) = Na. \tag{3.56}$$

Figure 3.1(c)–(d) shows that the average cell density, $\tilde{q}(x,t)$, and the average chemical concentration, $\tilde{\mathcal{C}}_1(x,t)$, approach the limits stated in Equation (3.56) as $t \to \infty$. The free boundary in Figure 3.1(a)–(b) demonstrates that $L(t)$ approaches the limit stated in Equation (3.56) as $t \to \infty$.

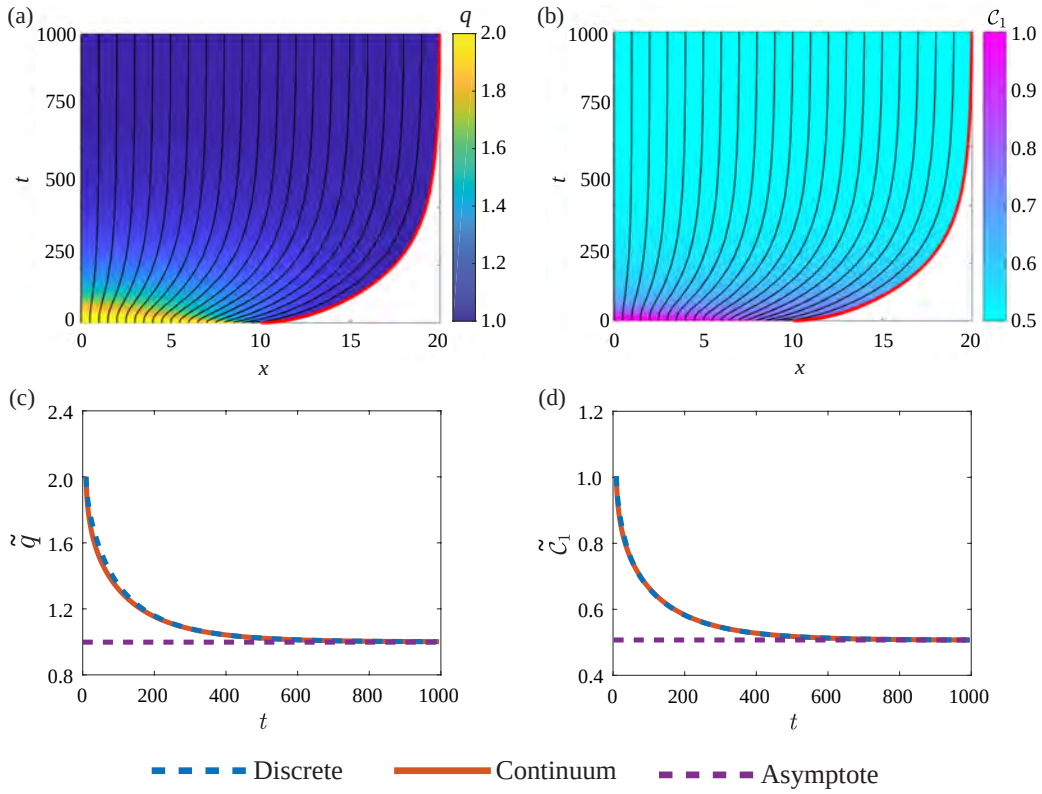

Figure 3.1: Homogeneous tissue consisting of one chemical species where $Z_1(\mathcal{C}_1) = 0$ and $a = k = D_1 = \eta = 1$. Characteristic diagrams in (a)–(b) illustrate the position of cell boundaries where the free boundary is highlighted in red. The colour in (a)–(b) represents $q(x,t)$ and $\mathcal{C}_1(x,t)$ respectively. Discrete and continuum solutions for the average cell density, $\tilde{q}(x,t)$, and the average chemical concentration, $\tilde{\mathcal{C}}_1(x,t)$ are compared in (c)–(d) respectively. The purple line in (c)–(d) shows the asymptotic behaviour of $\tilde{q}(x,t) = 1/a$ and $\tilde{\mathcal{C}}_1(x,t) = P/(Na)$ respectively.

3.4 Case study 1: Rac–Rho pathway

To investigate the Rac–Rho pathway, we let $\boldsymbol{\mathcal{C}}(x,t) = \{\mathcal{C}_1(x,t), \mathcal{C}_2(x,t)\}$ such that $\mathcal{C}_1(x,t)$ represents the concentration of RhoA and $\mathcal{C}_2(x,t)$ represents the concentration of Rac1. Figure 3.2 compares the discrete and continuum solutions relating to Figure 2.5.

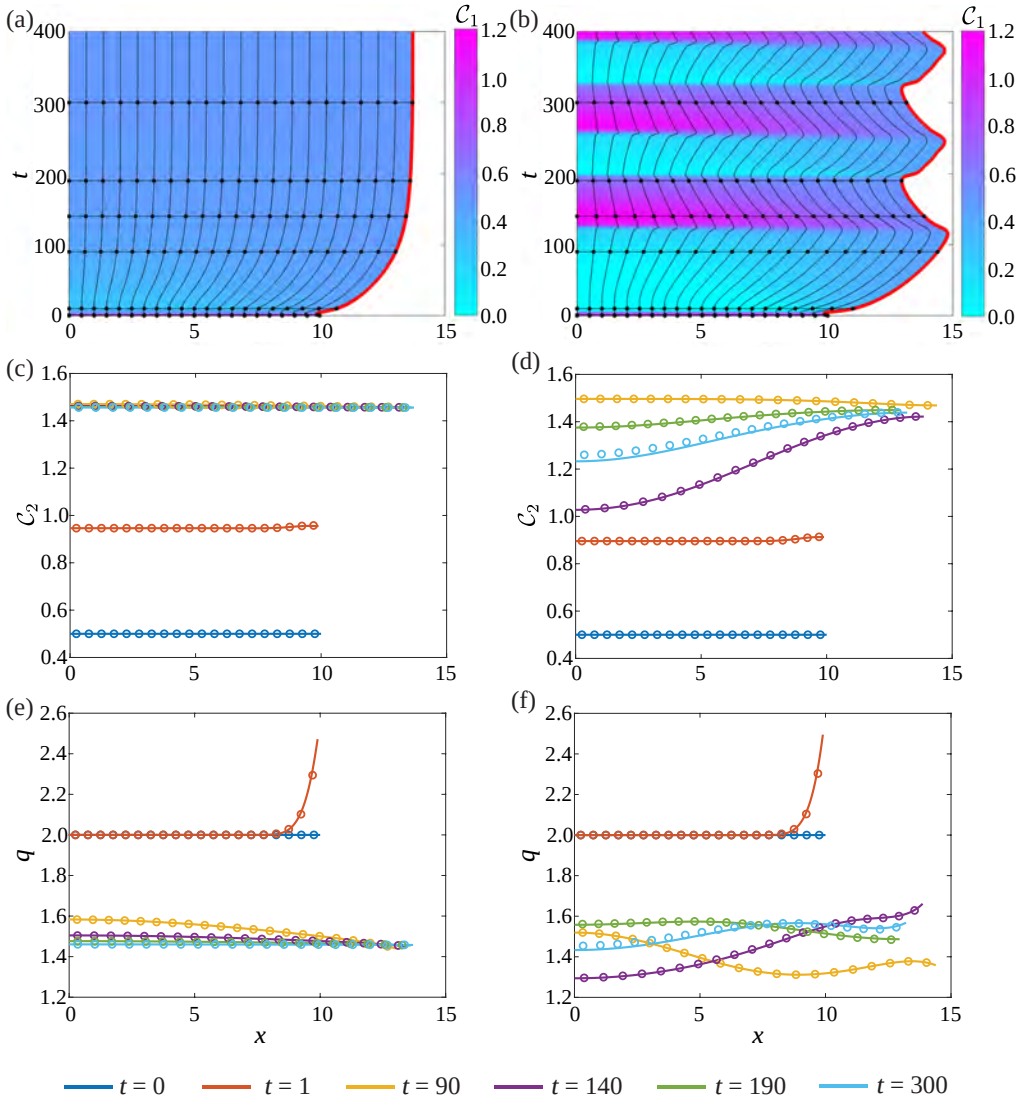

Figure 3.2: 1D tissue dynamics for the interaction of RhoA and Rac1. (a),(c),(e) correspond to non-oscillatory system where $\hat{\beta} = 1$ and (b),(d),(f) relate to an oscillatory system where $\hat{\beta} = 2.5$. Characteristic diagrams in (a)–(b) illustrate the behaviour of $\mathcal{C}_1(x,t)$ where the free boundary is highlighted in red. The black horizontal lines indicate times at which $\mathcal{C}_2(x,t)$ and $q(x,t)$ snapshots are shown in (c)–(d) and (e)–(f) respectively. In (c)–(f), the discrete and continuum solutions are compared as the dots and solid line respectively for $t = 0, 1, 90, 140, 190, 300$. In both systems, $a = l_0 - \phi\mathcal{C}_1^p / \left(G_h^p + \mathcal{C}_1^p\right)$, $k = 1 + 0.1\mathcal{C}_2$, $D_1 = D_2 = 1$ and $\eta = 1$. Parameters: $b_1 = b_2 = 1, \delta_1 = \delta_2 = 1, n = 3, p = 4, G_{1_\mathrm{T}} = 2, G_{2_\mathrm{T}} = 3, l_0 = 1, \phi = 0.65, G_h = 0.4$.

3.4.1 Single cell model

To investigate the influence of mechanobiological coupling on cellular dynamics, a discrete computational framework is used to model a single cell [60, 64]. We let $\mathbf{C}(t) = \left\{C^{(1)}(t), C^{(2)}(t)\right\}$ where $C^{(1)}(t)$ represents RhoA and $C^{(2)}(t)$ represents Rac1. As only a single cell is of interest, $\mathbf{C}(t)$ is not indexed with a subscript (Figure 3.3). Mechanobiological coupling is introduced such that the cell resting length, $a = a(\mathbf{C})$, and the cell stiffness, $k = k(\mathbf{C})$, depend on the chemical family, $\mathbf{C}(t)$.

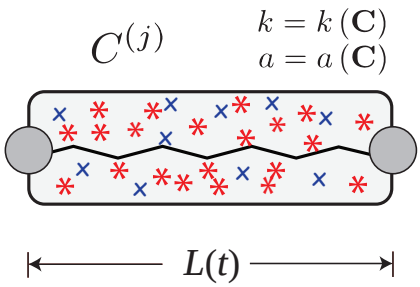

Figure 3.3: Schematic of a single cell with length $L(t)$. The mechanical cell properties, a and k, depend on the family of chemical signals, $\mathbf{C}(t) = \left\{C^{(1)}(t), C^{(2)}(t)\right\}$.

We model the cell as an overdamped, mechanical spring [31, 78] such that $\mathbf{C}(t)$ tends to decrease as the cell expands, and tends to increase as the cell compresses. Thus, the governing equations are,

$$\frac{\mathrm{d}L}{\mathrm{d}t} = -\varepsilon\left(L - a(\mathbf{C})\right), \tag{3.57}$$

$$\frac{\mathrm{d}C^{(j)}}{\mathrm{d}t} = \underbrace{Z^{(j)}(\mathbf{C})}_{\substack{\text{chemical}\\ \text{reactions}}} - \underbrace{\frac{C^{(j)}}{L}\frac{\mathrm{d}L}{\mathrm{d}t}}_{\substack{\text{changes in}\\ \text{cell length}}}, \tag{3.58}$$

where $L(t)$ is the cell length, $\varepsilon = 2k(\mathbf{C})/\eta$ is the rate of contraction, η is the mobility coefficient and $Z^{(j)}(\mathbf{C})$ governs the reactions between the chemical species within the cell [60]. For simplicity, the cell stiffness is chosen to be independent of $\mathbf{C}(t)$ such that ε is constant. The cell resting length is assumed to vary from a fixed value, l_0 [60]. By including a Hill function with amplitude ϕ, switch location G_{h} and power p, we assume RhoA shortens the resting cell length [60],

$$a(\mathbf{C}) = l_0 - \phi\frac{\left(C^{(1)}\right)^p}{G_{\mathrm{h}} + \left(C^{(1)}\right)^p}. \tag{3.59}$$

Equations (3.57) and (3.58) form a dynamical system. Phase planes are con-

structed to characterise the dependence of the system stability on the strength of the mechanobiological coupling. We used this analysis to inform our choice of model parameters in Chapter 2.3.2. The equilibrium points, $\bar{L}$ and $\bar{C}^{(j)}$, are determined by setting the time derivatives to zero such that $\bar{L} = a\left(\bar{\mathbf{C}}\right)$ and $Z^{(j)}\left(\bar{\mathbf{C}}\right) = 0$.

To investigate a single cell containing only RhoA, we consider $\mathbf{C}(t) = \left\{C^{(1)}(t)\right\}$ and let [60]

$$\begin{aligned} Z^{(1)}\left(\mathbf{C}\right) = &\overbrace{\left(b + \underbrace{\gamma\frac{\left(C^{(1)}\right)^n}{1+\left(C^{(1)}\right)^n}}_{\text{feedback loop}} + \underbrace{\beta\left(L(t) - a\left(C^{(1)}\right)\right)}_{\substack{\text{mechanobiological}\\ \text{coupling}}}\right)\left(G_{\mathrm{T}} - C^{(1)}\right)}^{\text{activation}} \\ &- \underbrace{\delta C^{(1)}}_{\text{deactivation}}, \end{aligned} \tag{3.60}$$

where b is the basal activation rate, γ is rate of feedback activation, β governs the strength of the mechanobiological coupling, G_{T} is the total amount of active and inactive RhoA, and δ is the deactivation rate [60, 64]. By substituting $\bar{L} = a\left(\bar{\mathbf{C}}\right)$ into $Z^{(1)}\left(\bar{C}^{(1)}\right) = 0$, $\bar{C}^{(1)}$ is numerically computed as the roots of,

$$\begin{aligned} 0 = &\left(-b - \gamma + \delta\right)\left(\bar{C}^{(1)}\right)^{n+1} + \left(bG_{\mathrm{T}} + \delta G_{\mathrm{T}}\right)\left(\bar{C}^{(1)}\right)^n \\ &+ \left(-b + \delta\right)\bar{C}^{(1)} + bG_{\mathrm{T}}. \end{aligned} \tag{3.61}$$

Equation (3.61) is independent of β. Thus, we vary β to investigate how the system stability depends on the strength of the mechanobiological coupling (Figure 3.4). Phase planes are constructed using `quiver` in MATLAB [98], and trajectories are computed using `ode15s` in MATLAB [81] (Figure 3.4).

Figure 3.4(a),(c) demonstrates that the equilibrium point is stable when $\beta = 0.2$, and the cell exhibits non-oscillatory behaviour. By increasing the strength of the mechanobiological coupling to $\beta = 0.3$, a limit cycle arises, which leads to continuous oscillations in $L(t)$ and $C^{(1)}(t)$ (Figure 3.4(b),(d)). Stability analysis reveals that the equilibrium point is unstable for $\beta = 0.3$. Thus, all solutions, regardless of the initial condition, exhibit oscillatory behaviour when $\beta = 0.3$ (Figure 3.4(b)).

To investigate how intracellular reactions between RhoA and Rac1 impact cell

behaviour, we consider $\mathbf{C}(t) = \left\{C^{(1)}(t), C^{(2)}(t)\right\}$ and let [60],

$$Z^{(1)}(\mathbf{C}) = \overbrace{\left(b_1 + \underbrace{\hat{\beta}\left(L(t) - a\left(C^{(1)}\right)\right)}_{\substack{\text{mechanobiological}\\ \text{coupling}}}\right)\frac{1}{1+\left(C^{(2)}\right)^n}\left(G_{1_\mathrm{T}} - C^{(1)}\right)}^{\text{activation}} - \underbrace{\delta_1 C^{(1)}}_{\text{deactivation}}, \tag{3.62}$$

$$Z^{(2)}(\mathbf{C}) = \underbrace{\frac{b_2}{1+\left(C^{(1)}\right)^n}\left(G_{2_\mathrm{T}} - C^{(2)}\right)}_{\text{activation}} - \underbrace{\delta_2 C^{(2)}}_{\text{deactivation}}, \tag{3.63}$$

where $C^{(1)}(t)$ is the concentration of RhoA and $C^{(2)}(t)$ is the concentration of Rac1. Figure 3.5(a),(c) illustrates that when the mechanobiological coupling is weak, $\hat{\beta} = 1$, the equilibrium point is stable and the cell mechanically relaxes. By increasing the strength of the mechanobiological coupling to $\hat{\beta} = 2.5$, a limit cycle arises and the cell exhibits oscillatory behaviour (Figure 3.5(b),(d)).

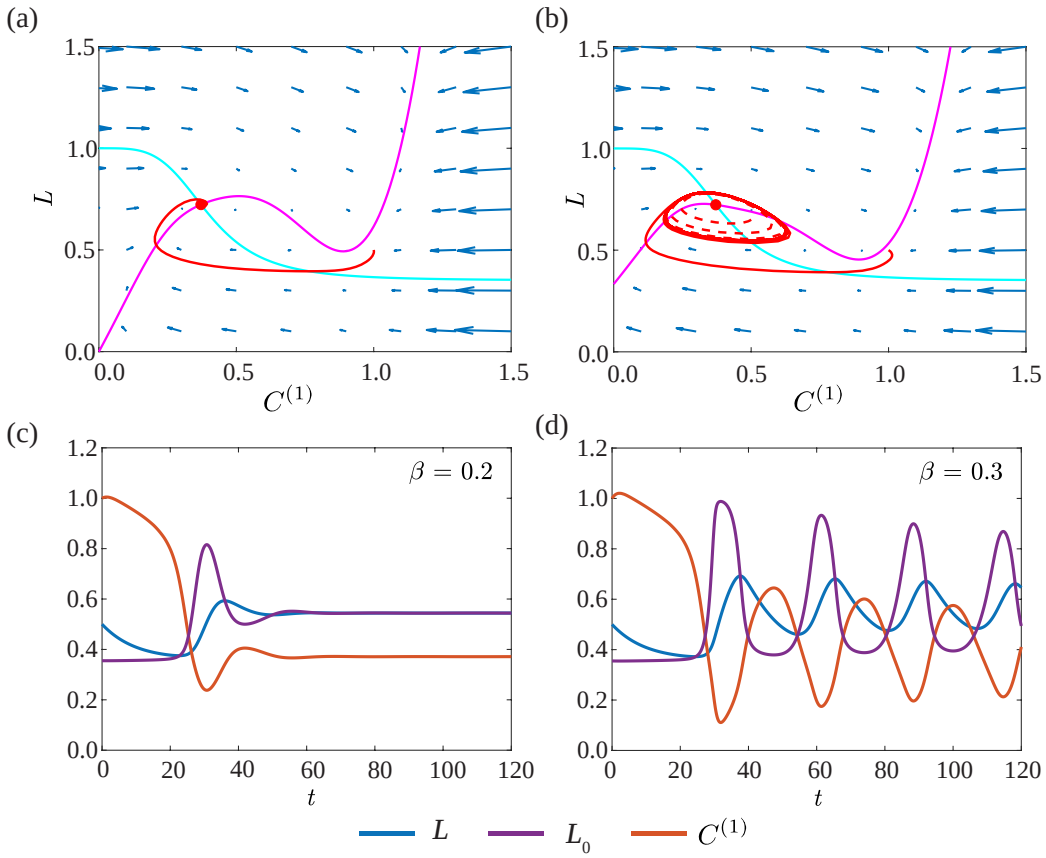

Figure 3.4: Dynamics of a single cell containing RhoA. (a),(c) corresponds to a non-oscillatory system where $\beta = 0.2$, and (b),(d) corresponds to an oscillatory system where $\beta = 0.3$. In (a)–(b), cyan represents the L nullcline and magenta represents the $C^{(1)}$ nullcline. The trajectory for $\left(C^{(1)}(0), L(0)\right) = (0.5, 1)$ is shown in red. In (b), the additional trajectory for $\left(C^{(1)}(0), L(0)\right) = (0.5, 0.65)$ is drawn as a dashed red line to demonstrate that all solutions exhibit oscillatory behaviour for $\beta = 0.3$. Parameters are: $b = 0.2, \gamma = 1.5, n = 4, p = 4, G_{\mathrm{T}} = 2, l_0 = 1, \phi = 0.65, G_{\mathrm{h}} = 0.4, \delta = 1, \varepsilon = 0.1$.

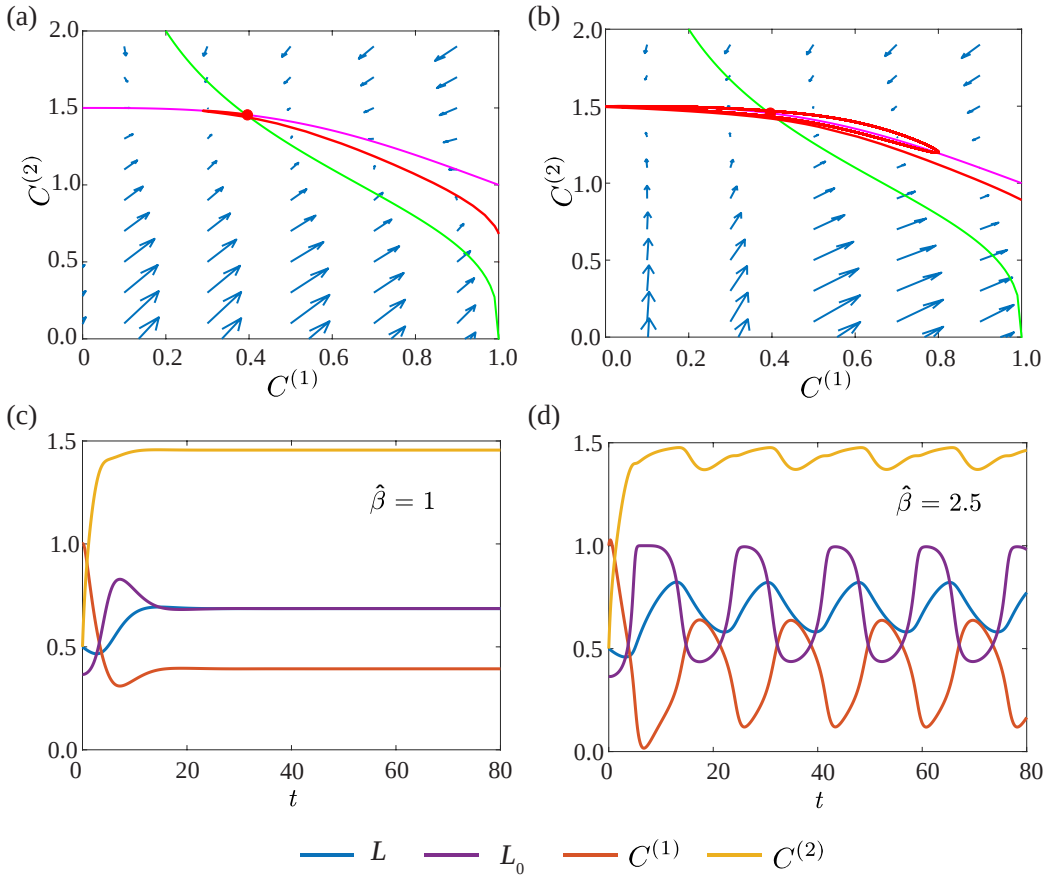

Figure 3.5: Reactions between RhoA and Rac1 in a single cell. (a),(c) corresponds to a non-oscillatory system where $\hat{\beta} = 1$, and (b),(d) corresponds to an oscillatory system where $\hat{\beta} = 2.5$. In (a)–(b), magenta represents the $C^{(1)}$ nullcline and green represents the $C^{(2)}$ nullcline. The trajectory for $\left(L(0), C^{(1)}(0), C^{(2)}(0)\right) = (0.5, 1, 0.5)$ in shown in red. Parameters: $b_1 = b_2 = 1, \delta_1 = \delta_2 = 1, n = 3, p = 4, G_{1_{\mathrm{T}}} = 2, G_{2_{\mathrm{T}}} = 3, l_0 = 1, \phi = 0.65, G_{\mathrm{h}} = 0.4, \varepsilon = 0.1$.

3.5 Case study 2: Activator–inhibitor patterning

Chapter 2.3.3 considers an activator–inhibitor system with $\boldsymbol{\mathcal{C}}(x,t) = \{\mathcal{C}_1(x,t), \mathcal{C}_2(x,t)\}$, where $\mathcal{C}_1(x,t)$ is the activator and $\mathcal{C}_2(x,t)$ is the inhibitor. Figure 3.6 illustrates the long time behaviour of Figure 2.6(b),(d). Figure 3.6 demonstrates that two distinct activator peaks evolve as $t \to \infty$ when $d > d_c$. Thus, unlike [51,52], we do not observe continuous peak splitting.

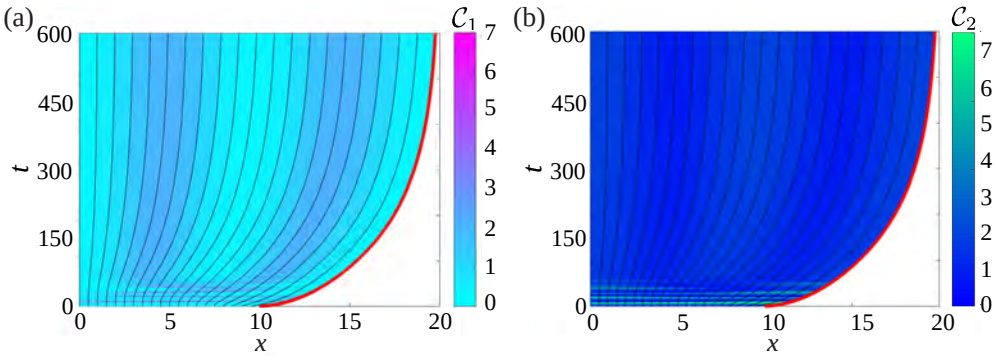

Figure 3.6: The evolution of spatial–temporal patterns in a homogeneous tissue with Schnakenberg dynamics, where $D_1 = 0.5$ and $D_2 = 5$ such that $d > d_c$. (a) illustrates the behaviour of the activator, $\mathcal{C}_1(x,t)$, and (b) illustrates the behaviour of the inhibitor, $\mathcal{C}_2(x,t)$. Parameters are as in Figure 2.6.

Chapter 4

Conclusion

4.1 Summary

In this thesis, a novel free boundary mechanobiological model of epithelial tissues is derived. Cell migration within epithelial tissues is studied by considering the boundaries between adjacent cells, where the moving cell front is modelled as a free boundary. One of the main outcomes of this research is including mechanobiological coupling in a free boundary model of epithelial tissues. Previous studies investigate mechanical cell properties [29–31, 61, 62], or chemical signals [35, 43, 60, 63] in epithelial tissues. In this study, cell–based mechanical properties are coupled to intracellular signalling in a free boundary model, to study their combined effect on the evolution of epithelial tissues.

In Chapter 2, a free boundary mechanobiological model of epithelial tissues is developed in both a discrete and continuum modelling framework. One key feature of this research is the derivation of the free boundary condition in the continuum model. Some existing continuum models pre-specify the rate of tissue elongation [48–52], or describe the free boundary using a one–phase Stefan condition [53, 54]. Other continuum models which consider tumour spheroids couple the free boundary condition to the local nutrient concentration [55–57]. In contrast, the free boundary condition presented in this study arises due to the underlying biological mechanisms and mechanobiological coupling included in the discrete model. As such, the free boundary model is applicable to non-uniformly evolving tissues, and appropriately describes the evolution of heterogeneous cell populations. Thus, this research extends and unifies existing mathematical models of epithelial tissues.

Extensive numerical exploration in Chapter 2 demonstrates that the continuum model and free boundary condition successfully capture the underlying biological

mechanisms included in the discrete model. Additional results and analysis in Chapter 3 compliment the findings of Chapter 2.

4.2 Discussion

In this research, mechanobiological coupling is investigated at the cell level in a discrete modelling framework, and the continuum model is derived to describe tissue–level outcomes. The cell–based model consists of a system of coupled, ordinary differential equations which describe the mechanical relaxation of cells, chemical reactions within cells, and diffusive transport between nearest neighbour cells. The continuum model is derived as a system of coupled, non-linear partial differential equations. While continuum models can be derived using a variety of coarse–graining techniques [11, 29–31, 44], the continuum model in this work is derived by assuming that $N \to \infty$. As epithelial tissues consist of extensive layers of cells [25], this assumption is biologically reasonable. We further assume that the mechanical relaxation of cells is sufficiently fast. This assumption is also appropriate as the timescale of mechanical relaxation is much faster than the timescale of other cellular mechanisms, such as proliferation [99].

The accuracy of the continuum model, including the free boundary condition, is investigated by comparing numerical solutions from the discrete and continuum models relating to different biological scenarios. Preliminary results replicate the work of Baker et al. [30] by considering a homogeneous cell population with no mechanobiological coupling. In doing so, we find that the free boundary condition derived in Chapter 2 reduces to the free boundary condition derived in Baker et al. [30]. Numerical results in Chapters 2 and 3 demonstrate excellent agreement between the solutions of the discrete and continuum models. Thus, the continuum model accurately describes the dynamics of homogeneous cell populations with no mechanobiological coupling.

To investigate the accuracy of the continuum model in epithelial tissues with mechanobiological coupling, the model is applied in two case studies relating to different signalling pathways. The first case study considers the Rac–Rho pathway and investigates how RhoA and Rac1 influence the evolution of epithelial tissues. The work of Zmurchok et al. [60] is extended by investigating how oscillatory and non-oscillatory tissue dynamics arise as a result of mechanobiological coupling. The oscillatory tissue dynamics provide a challenging scenario to test the accuracy of the free boundary condition in describing non-uniform tissue evolution. Phase plane analysis in Chapter 3 investigates how the model parameters affect the dynamics of the tissue. We find that non-oscillatory tissue dynamics relate to a stable

fixed point, whereas oscillatory tissue dynamics relate to an unstable fixed point enclosed by a limit cycle. The effect of diffusion on tissue dynamics is investigated, and we find that increasing the diffusion coefficient does not significantly dampen the oscillations, but introduces a temporal phase shift. In all test cases, excellent agreement between solutions of the discrete and continuum models is observed.

The second case study considers the formation of activator–inhibitor patterns on an evolving cellular domain. Schnakenberg kinetics are used to characterise the pattern splitting observed on the skin of angelfish. As the free boundary condition derived in the continuum model describes non-uniform tissue evolution, the development of spatial–temporal patterns on a non-uniformly evolving cellular domain is investigated. In doing so, we extend previous studies which consider spatial–temporal patterns on uniformly evolving domains [51,52,73,74]. Numerical results in Chapters 2 and 3 show splitting in the activator peaks, and demonstrate agreement between the solutions of the discrete and continuum models.

Baker et al. [30] show that the accuracy of continuum models increase as $N \to \infty$ [30]. One potential approach to improve the accuracy of the continuum model is to retain additional terms in the truncated Taylor series used to derive the continuum model. We do not follow this approach for two reasons. First, retaining higher order terms can lead to ill–posed partial differential equation models [100]. Second, extensive numerical exploration in Chapters 2 and 3 justify that the continuum model and the free boundary condition accurately reflect the biological mechanisms included in the discrete model, for a relatively small value of $N = 20$. Therefore, we conclude that retaining additional terms in the truncated Taylor series when deriving the continuum model is not required in this study.

4.3 Future research

In deriving the discrete and continuum models, certain assumptions were made to simplify aspects of the models. These assumptions are now addressed as extensions of this work and opportunities for future research.

In constructing the model, a linear force law is chosen to describe cell-to-cell interactions within the tissue. This choice is reasonable as it successfully captures the mechanical properties of cells, such as resistance to deformation and cell size. Non-linear force laws such as the cubic or Hertz force law could be used to expand the range of potential cell-to-cell interactions, and to capture the effect of large separations between cells in epithelial tissues [30, 61]. Existing mathematical models which consider non-linear force laws often extend previous studies which use a linear force [30, 61]. Thus, this study presents a good foundation and

modelling framework to include non-linear force laws. We anticipate that using a non-linear force law will significantly affect the free boundary condition. Thus, care is warranted when deriving the free boundary condition in the continuum model to ensure that it reflects the discrete model.

In developing the discrete model, an unbiased, position–jump process is chosen to describe diffusive chemical transport between neighbouring cells. The length– and time–dependent transport rates are further chosen to correspond to a linear diffusion mechanism in the continuum model. Other possibilities for describing diffusive chemical transport at the cell level include biased, position–jump processes. Some position–jump processes include a global directional bias to incorporate the effects of drift [93]. These processes correspond to the advection–diffusion equation at the macroscopic level [93], and offer an alternative way to model chemical transport within epithelial tissues.

Another extension of this work is to include cell proliferation and cell death. Cell proliferation and death play crucial roles in tumour development as cancerous cells are thought to proliferate at a higher rate than healthy cells, and healthy cells commonly die due to the invasion of cancerous cells [101]. Cell proliferation is also important in wound healing as cells are known to proliferate in the vicinity of open wounds [102]. Previous studies investigate the role of cell proliferation and mechanical cell properties in epithelial tissues [30, 38]. Baker et al. [30] include cell proliferation in a free boundary model for homogeneous cell populations, whereas Murphy et al. [38] consider cell proliferation in heterogeneous tissues of fixed length. These studies assume that cells proliferate stochastically at a rate which depends on the current length of the cell [30,38]. We present a general modelling framework with mechanobiological coupling which could extend to include cell proliferation that depends on the chemical properties of cells. In doing so, a free boundary mechanobiological model with cell proliferation which applies to heterogeneous cell populations could be developed. This extension may lead to a model which is applicable to biochemical networks where biological mechanisms regulate the proliferation of cells in epithelial tissues [95]. Cell death could be incorporated in a similar fashion. Thus, by including cell proliferation and death in the free boundary model presented in this thesis, tumour development and wound healing can be further investigated.

In considering mechanobiological coupling in epithelial tissues, specific signalling pathways that consist of one or two chemical species are investigated. While Schnakenberg kinetics model the splitting of activator peaks, other activator–inhibitor interactions, such as Gierer–Meinhardt kinetics, can be used to investigate the insertion of new activator peaks [51, 52, 73]. As this study considers an

epithelial tissue consisting of a family of chemicals species, the model can be applied to case studies involving more than two chemicals species. In particular, the free boundary model can be used to capture the role and interaction of other members of the Rho GTPase family, such as RhoC, Rac2 and Cdc42, which contribute to wound healing and tumour development [70, 84].

This study demonstrates the potential of mathematical models to investigate mechanobiological coupling in epithelial tissues. In extending the free boundary model presented in this thesis and expanding its applications, mechanobiological coupling in epithelial tissues can be further investigated.

Bibliography

[1] Murray J. 2002. *Mathematical Biology*. New York: Springer.

[2] Edelstein-Keshet L. 2005. *Mathematical Models in Biology*. Philadelphia: Society for Industrial and Applied Mathematics SIAM.

[3] Riahi R, Yang Y, Zhang DD, Wong PK. 2012. Advances in wound-healing assays for probing collective cell migration. *Journal of Laboratory Automation*. **17**, 59–65. (doi: 10.1177/2211068211426550).

[4] Li L, He Y, Zhao M, Jiang J. 2013. Collective cell migration: implications for wound healing and cancer invasion. *Burns & Trauma*. **1**, 2321–3868. (doi: 10.4103/2321-3868.113331).

[5] Sherratt JA, Murray JD. 1990. Models of epidermal wound healing. *Proceedings of the Royal Society of London, Series B: Biological Sciences*. **241**, 29–36. (doi: 10.1098/rspb.1990.0061).

[6] Swanson KR, Bridge C, Murray JD, Alvord Jr EC. 2003. Virtual and real brain tumors: using mathematical modeling to quantify glioma growth and invasion. *Journal of the Neurological Sciences*. **216**, 1–10. (doi: 10.1016/j.jns.2003.06.001).

[7] Jonkman JE, Cathcart JA, Xu F, Bartolini ME, Amon JE, Stevens KM, Colarusso P. 2014. An introduction to the wound healing assay using live-cell microscopy. *Cell Adhesion & Migration*. **8**, 440–451. (doi: 10.4161/cam.36224).

[8] Liang C, Park A. Guan J. 2007. *In vitro* scratch assay: a convenient and inexpensive method for analysis of cell migration in vitro. *Nature Protocols*. **2**, 329–333. (doi: 10.1038/nprot.2007.30).

[9] Vittadello ST, McCue SW, Gunasingh G, Haass NK, Simpson MJ. 2018. Mathematical models for cell migration with real-time cell cycle dynamics. *Biophysical Journal*. **114**, 1241–1253. (doi: 10.1016/j.bpj.2017.12.041).

[10] Johnston ST, Simpson MJ, McElwain DLS. 2014. How much information can be obtained from tracking the position of the leading edge in a scratch assay? *Journal of the Royal Society Interface*. **11**, 20140325. (doi: 10.1098/rsif.2014.0325).

[11] Matsiaka OM, Penington CJ, Baker RE, Simpson MJ. 2018. Discrete and continuum approximations for collective cell migration in a scratch assay with cell size dynamics. *Bulletin of Mathematical Biology*. **80**, 738–757. (doi: 10.1007/s11538-018-0398-2).

[12] Jin W, Shah ET, Penington CJ, McCue SW, Chopin LK, Simpson MJ. 2016. Reproducibility of scratch assays is affected by the initial degree of confluence: experiments, modelling and model selection. *Journal of Theoretical Biology*. **390**, 136–145. (doi: 10.1016/j.jtbi.2015.10.040).

[13] Simpson MJ, Treloar KK, Binder BJ, Haridas P, Manton KJ, Leavesley DI, McElwain DLS, Baker RE. 2013. Quantifying the roles of cell motility and cell proliferation in a circular barrier assay. *Journal of the Royal Society Interface*. **10**, 20130007. (doi: 10.1098/rsif.2013.0007).

[14] Simpson MJ, Jin W, Vittadello ST, Tambyah TA, Ryan JM, Gunasingh G, Haass NK, McCue SW. 2018. Stochastic models of cell invasion with fluorescent cell cycle indicators. *Physica A: Statistical Mechanics and its Applications*. **510**, 375–386.

[15] Jin W, Shah ET, Penington CJ, McCue SW, Maini PK, Simpson MJ. 2017. Logistic proliferation of cells in scratch assays is delayed. *Bulletin of Mathematical Biology*. **79**, 1028–1050. (doi: 10.1007/s11538-017-0267-4).

[16] Fisher RA. 1937. The wave of advance of advantageous genes. *Annals of Eugenics*. **7**, 355–369. (doi: 10.1111/j.1469-1809.1937.tb02153.x).

[17] Kolmogorov AN, Petrovskii IG, Piskunov NS, 1937. A study of the diffusion equation with increase in the amount of substance, and its application to a biological problem. *Moscow University Bulletin of Mathematics*. **1**, 1–25.

[18] Swanson K, Rostomily R, Alvord E. 2008. A mathematical modelling tool for predicting survival of individual patients following resection of glioblastoma: a proof of principle. *British Journal of Cancer*. **98**, 113–119. (doi: 10.1038/sj.bjc.6604125).

[19] Gerlee P, Nelander S. 2012. The impact of phenotypic switching on glioblastoma growth and invasion. *PLoS Computational Biology*. **8**, e1002556. (doi: 10.1371/journal.pcbi.1002556).

[20] Maini PK, McElwain DS, Leavesley DI. 2004. Traveling wave model to interpret a wound-healing cell migration assay for human peritoneal mesothelial cells. *Tissue Engineering*. **10**, 475–482. (doi: 10.1089/107632704323061834).

[21] Sherratt JA. 1998. On the transition from initial data to travelling waves in the Fisher-KPP equation. *Dynamics and Stability of Systems*. **13**, 167–174. (doi: 10.1080/02681119808806258).

[22] Maini PK, McElwain DLS, Leavesley D. 2004. Travelling waves in a wound healing assay. *Applied Mathematics Letters*. **17**, 575–580. (doi: 10.1016/S0893-9659(04)90128-0).

[23] Fristrom D. 1988. The cellular basis of epithelial morphogenesis. A review. *Tissue and Cell*. **20**, 645–690. (doi: 10.1016/0040-8166(88)90015-8).

[24] Freshney RI, Freshney MG. 2002. *Culture of Epithelial Cells*. New York: John Wiley & Sons.

[25] Betts JG, Desaix P, Johnson E, Johnson JE, Korol O, Kruse D, Poe B, Wise JA, Womble M, Young KA. 2017. *Anatomy and Physiology*. Houston: Rice University.

[26] Schock F, Perrimon N. 2002. Molecular mechanisms of epithelial morphogenesis. *Annual Review of Cell and Developmental Biology*. **18**, 463–493. (doi: 10.1146/annurev.cellbio.18.022602.131838).

[27] Guillot C, Lecuit T. 2013. Mechanics of epithelial tissue homeostasis and morphogenesis. *Science*. **340**, 1185–1189. (doi: 10.1126/science.1235249).

[28] Xu GK, Liu Y, Li B. 2015. How do changes at the cell level affect the mechanical properties of epithelial monolayers? *Soft Matter*. **11**, 8782–8788. (doi: 10.1039/c5sm01966d).

[29] Murphy RJ, Buenzli PR, Baker RE, Simpson MJ. 2019. An individual–based mechanical model of cell movement in heterogeneous tissues and its coarse–grained approximation. *Proceedings of the Royal Society A: Mathematical, Physical and Engineering Sciences.* **475**, 20180838. (doi: 10.1101/485276).

[30] Baker RE, Parker A, Simpson MJ. 2019. A free boundary model of epithelial dynamics. *Journal of Theoretical Biology.* **481**, 61–74. (doi: 10.1016/j.jtbi.2018.12.025).

[31] Murray PJ, Edwards CM, Tindall MJ, Maini PK. 2009. From a discrete to a continuum model of cell dynamics in one dimension. *Physical Review E: Statistical, Nonlinear, and Soft Matter Physics.* **80**, 031912. (doi: 10.1103/PhysRevE.80.031912).

[32] Dasbiswas K, Hannezo E, Gov NS. 2018. Theory of epithelial cell shape transitions induced by mechanoactive chemical gradients. *Biophysical Journal.* **114**, 968–977. (doi: 10.1016/j.bpj.2017.12.022).

[33] Fernandez-Sanchez ME, Brunet T, Roper JC, Farge E. 2015. Mechanotransduction's impact on animal development, evolution, and tumorigenesis. *Annual Review of Cell and Developmental Biology.* **31**, 373–397. (doi: 10.1146/annurev-cellbio-102314-112441).

[34] Jin S. 2019. Bipotent stem cells support the cyclical regeneration of endometrial epithelium of the murine uterus. *Proceedings of the National Academy of Sciences of the United States of America.* **116**, 6848–6857. (doi: 10.1073/pnas.1814597116).

[35] Osborne JM, Fletcher AG, Pitt-Francis JM, Maini PK, Gavaghan DJ. 2017. Comparing individual–based approaches to modelling the self–organization of multicellular tissues. *PLoS Computational Biology.* **13**, e1005387. (doi: 10.1371/journal.pcbi.1005387).

[36] Pathmanathan P, Cooper J, Fletcher AG, Mirams G, Murray PJ, Osborne JM, Pitt-Francis J, Walter A, Chapman SJ. 2009. A computational study of discrete mechanical tissue models. *Physical Biology.* **6**, 036001. (doi: 10.1088/1478-3975/6/3/036001).

[37] Graner F, Glazier JA. 1992. Simulation of biological cell sorting using a two-dimensional extended Potts model. *Physical Review Letters.* **69**, 2013. (doi: 10.1103/PhysRevLett.69.2013).

[38] Murphy RJ, Buenzli PR, Baker RE, Simpson, MJ. 2020. Mechanical cell competition in heterogeneous epithelial tissues. To appear, *Bulletin of Mathematical Biology.* Available on bioRxiv:869495. (doi: 10.1101/869495).

[39] Armstrong NJ, Painter KJ, Sherratt JA. 2006. A continuum approach to modelling cell–cell adhesion. *Journal of Theoretical Biology.* **243**, 98–113. (doi: 10.1016/j.jtbi.2006.05.030).

[40] Murphy RJ, Buenzli PR, Baker RE, Simpson MJ. 2020. Travelling waves in a free boundary mechanobiological model of an epithelial tissue. To appear, *Applied Mathematics Letters*. (doi: 10.1016/j.aml.2020.106636).

[41] Buttenschon A, Liu Y, Edelstein-Keshe, L. 2020. Cell size, mechanical tension, and GTPase signaling in the single cell. *Bulletin of Mathematical Biology.* **82**, 28. (doi: 10.1007/s11538-020-00702-5).

[42] Zmurchok C, Holmes WR. 2020. Simple Rho GTPase dynamics generate a complex regulatory landscape associated with cell shape. *Biophysical Journal.* **118**, 1438–1454. (doi: 10.1016/j.bpj.2020.01.035).

[43] Zmurchok C, Collette J, Rajagopal V, Holmes WR. 2020. Membrane tension can enhance adaptation to maintain polarity of migrating cells. Preprint on bioRxiv:2020.04.01.020289. (doi: 10.1101/2020.04.01.020289).

[44] Fozard JA, Byrne HM, Jensen OE, King JR. 2010. Continuum approximations of individual–based models for epithelial monolayers. *Mathematical Medicine and Biology.* **27**, 39–74. (doi: 10.1093/imammb/dqp015).

[45] Evans ND, Oreffo RO, Healy E, Thurner PJ, Man YH. 2013. Epithelial mechanobiology, skin wound healing, and the stem cell niche. *Journal of the Mechanical Behaviour of Biomedical Materials.* **28**, 397–409. (doi: 10.1016/j.jmbbm.2013.04.023).

[46] Fletcher AG, Cooper F, Baker RE. 2017. Mechanocellular models of epithelial morphogenesis. *Philosophical Transactions of the Royal Society B: Biological Sciences.* **372**, 20150519. (doi: 10.1098/rstb.2015.0519).

[47] Friedman A. 2015. Free boundary problems in biology. *Philosophical Transactions of the Royal Society A: Mathematical, Physical and Engineering Sciences.* **373**, 20140368. (doi: 10.1098/rsta.2014.0368).

[48] Simpson MJ, Landman KA, Newgreen DF. 2006. Chemotactic and diffusive migration on a nonuniformly growing domain: numerical algorithm development and applications. *Journal of Computational and Applied Mathematics.* **192**, 282–300. (doi: 10.1016/j.cam.2005.05.003).

[49] Simpson MJ, Sharp JA, Baker RE. 2015. Survival probability for a diffusive process on a growing domain. *Physical Review E: Statistical, Nonlinear, and Soft Matter Physics*. **91**, 042701. (doi: 10.1103/PhysRevE.91.042701).

[50] Simpson MJ, Baker RE. 2015. Exact calculations of survival probability for diffusion on growing lines, disks, and spheres: the role of dimension. *The Journal of Chemical Physics*. **143**, 094109. (doi: 10.1063/1.4929993).

[51] Maini PK, Woolley TE, Baker RE, Gaffney EA, Lee SS. 2012. Turing's model for biological pattern formation and the robustness problem. *Interface Focus.* **2**, 487–496. (doi: 10.1098/rsfs.2011.0113).

[52] Crampin EJ, Hackborn WW, Maini PK. 2002. Pattern formation in reaction–diffusion models with non-uniform domain growth. *Bulletin of Mathematical Biology.* **64**, 747–769. (doi: 10.1006/bulm.2002.0295).

[53] El-Hachem M, McCue SW, Wang J, Yihong D, Simpson MJ. 2019. Revisiting the Fisher–Kolmogorov–Petrovsky–Piskunov equation to interpret the spreading–extinction dichotomy. *Proceedings of the Royal Society A: Mathematical, Physical and Engineering Sciences.* **475**, 20190378. (doi: 10.1098/rspa.2019.0378).

[54] Du Y, Lin Z. 2010. Spreading-vanishing dichotomy in the diffusive logistic model with a free boundary. *SIAM Journal on Mathematical Analysis*. **42**, 377–405. (doi: 10.1137/090771089).

[55] Greenspan HP. 1972. Models for the growth of a solid tumor by diffusion. *Studies in Applied Mathematics*. **51**, 317–340. (doi: 10.1002/sapm1972514317).

[56] Ward JP, King JR. 1997. Mathematical modelling of avascular-tumour growth. *IMA Journal of Mathematics Applied in Medicine and Biology*. **14**, 39–69.

[57] Byrne HM, Chaplain MA. 1997. Free boundary value problems associated with the growth and development of multicellular spheroids. *European Journal of Applied Mathematics*. **8**, 639–658. (doi: 10.1017/S0956792597003264).

[58] Han YL, Pegoraro AF, Li H, Li K, Kaifu L, Yuan Y, Xu G, Gu Z, Sun J, Hao Y, Gupta SK, Li Y, Tang W, Kang H, Teng L, Fredberg JJ, Guo M. 2019. Cell swelling, softening and invasion in a three-dimensional breast cancer model. *Nature Physics*. **16**, 101–108. (doi: 10.1038/s41567-019-0680-8).

[59] Plodinec M, Loparic M, Monnier CA, Obermann EC, Zanetti-Dallenbach R, Oertle P, Hyotyla JT, Aebi U, Bentires-Alj M, Lim RYH, Schoenenberger, CA. 2012. The nanomechanical signature of breast cancer. *Nature Nanotechnology.* **7**, 757. (doi: 10.1038/nnano.2012.167).

[60] Zmurchok C, Bhaskar D, Edelstein-Keshet L. 2018. Coupling mechanical tension and GTPase signalling to generate cell and tissue dynamics. *Physical Biology.* **15**, 046004. (doi: 10.1088/1478-3975/aab1c0).

[61] Murray PJ, Edwards CM, Tindall MJ, Maini PK. 2012. Classifying general non-linear force laws in cell–based models via the continuum limit. *Physical Review E: Statistical, Nonlinear, and Soft Matter Physics.* **85**, 021921. (doi: 10.1103/PhysRevE.85.021921).

[62] Lorenzi T, Murray PJ, Ptashnyk M. 2019. From individual–based mechanical models of multicellular systems to free–boundary problems. Preprint on arXiv:1903.06590.

[63] Smith AM, Baker RE, Kay D, Maini PK. 2012. Incorporating chemical signalling factors into cell–based models of growing epithelial tissues. *Journal of Mathematical Biology.* **65**, 441–463. (doi: 10.1007/s00285-011-0464-y).

[64] Bui J, Conway DE, Heise RL, Weinberg SH. 2019. Mechanochemical coupling and junctional forces during collective cell migration. *Biophysical Journal.* **117**, 170–183. (doi: 10.1016/j.bpj.2019.05.020).

[65] Holmes WR, Park J, Levchenko A, Edelstein-Keshet L. 2017. A mathematical model coupling polarity signalling to cell adhesion explains diverse cell migration patterns. *PLoS Computational Biology.* **13**, e1005524. (doi: 10.1371/journal.pcbi.1005524).

[66] Byrne KM, Monsefi N, Dawson JC, Degasperi A, Bukowski-Wills J, Volinsky N, Dobrzynski M, Birtwistle MR, Tsyganov MA, Kiyatkin A, Kida K, Finch AJ, Carragher NO, Kolch W, Nguyen LK, von Kriegsheim A, Kholodenko BN. 2016. Bistability in the Rac1, PAK, and RhoA signalling network drives actin cytoskeleton dynamics and cell motility switches. *Cell Systems.* **2**, 38–48. (doi: 10.1016/j.cels.2016.01.003).

[67] Ridley AJ. 2001. Rho family proteins: coordinating cell responses. *Trends in Cell Biology.* **11**, 471–477. (doi: 10.1016/s0962-8924(01)02153-5).

[68] Guilluy C, Garcia-MataR, Burridge K. 2011. Rho protein crosstalk: another social network? *Trends in Cell Biology.* **21**, 718–726. (doi: 10.1016/j.tcb.2011.08.002).

[69] Samuel MS, Lopez JI, McGhee EJ, Croft DR, Strachan D, Timpson P, Munro J, Schroder E, Zhou J, Brunton VG, Barker N, Clevers H, Sansom OJ, Anderson KI, Weaver VM, Olson MF. 2011. Actomyosin–mediated cellular tension drives increased tissue stiffness and β-catenin activation to induce epidermal hyperplasia and tumour growth. *Cancer Cell.* **19**, 776–791. (doi: 10.1016/j.ccr.2011.05.008).

[70] Vega FM, Ridley AJ. 2008. Rho GTPases in cancer cell biology. *FEBS Letters.* **582**, 2093–2101. (doi: 10.1016/j.febslet.2008.04.039).

[71] Sahai E, Marshall CJ. 2002. RHO–GTPases and cancer. *Nature Reviews Cancer.* **2**, 133–142. (doi: 10.1038/nrc725).

[72] Kondo S, Asai R. 1995. A reaction–diffusion wave on the skin of the marine angelfish Pomacanthus. *Nature.* **376**, 765–768. (doi: 10.1038/376765a0).

[73] Crampin EJ, Gaffney EA, Maini PK. 1999. Reaction and diffusion on growing domains: scenarios for robust pattern formation. *Bulletin of Mathematical Biology.* **61**, 1093–1120. (doi: 10.1006/bulm.1999.0131).

[74] Crampin EJ, Gaffney EA, Maini PK. 2002. Mode–doubling and tripling in reaction–diffusion patterns on growing domains: a piecewise linear model. *Journal of Mathematical Biology.* **44**, 107–128. (doi: 10.1007/s002850100112).

[75] Boocock D, Hino N, Ruzickova N, Hirashima T, Hannezo E. Theory of mechano–chemical patterning and optimal migration in cell monolayers. Preprint on bioRxiv:096479. (doi: 10.1101/2020.05.15.096479).

[76] Serra-Picamal, X, Conte V. Vincent R, Anon E, Tambe DT, Bazellieres E, Butler JP, Fredberg JJ, Trepat X. 2012. Mechanical waves during tissue expansion. *Nature Physics.* **8**, 628–634. (doi: 10.1038/NPHYS2355).

[77] Dalwadi MP, Waters SL, Byrne HM, Hewitt IJ. 2020. A mathematical framework for developing freezing protocols in the cryopreservation of cells. *SIAM Journal on Applied Mathematics.* **80**, 657–689. (doi: 10.1137/19M1275875).

[78] Matsiaka OM, Penington CJ, Baker RE, Simpson MJ. 2017. Continuum approximations for lattice–free multi–species models of collective cell migration. *Journal of Theoretical Biology.* **422**, 1–11. (doi: 10.1016/j.jtbi.2017.04.009).

[79] Painter KJ, Sherratt JA. 2003. Modelling the movement of interacting cell populations. *Journal of Theoretical Biology.* **225**, 327–339. (doi: 10.1016/S0022-5193(03)00258-3).

[80] Yates CA, Baker RE, Erban R, Maini PK. 2012. Going from microscopic to macroscopic on non-uniform growing domains. *Physical Review E: Statistical, Nonlinear, and Soft Matter Physics.* **86**, 21921. (doi: 10.1103/PhysRevE.86.021921).

[81] MathWorks `ode15s`. Retrieved from https://au.mathworks.com/help/matlab/ref/ode15s.html in July 2020.

[82] Simpson MJ. 2020. Critical length for the spreading–vanishing dichotomy in higher dimensions. *ANZIAM Journal.* 1–15. (doi: 10.1017/S1446181120000103).

[83] Holmes WR, Edelstein-Keshet L. 2016. Analysis of a minimal Rho–GTPase circuit regulating cell shape. *Physical Biology.* **13**, 046001. (doi: 10.1088/1478-3975/13/4/046001).

[84] Abreu-Blanco MT, Verboon JM, Parkhurst SM. 2014. Coordination of Rho family GTPase activities to orchestrate cytoskeleton responses during cell wound repair. *Current Biology.* **24**, 144–155. (doi: 10.1016/j.cub.2013.11.048).

[85] Clayton NS, Ridley AJ. 2020. Targeting Rho GTPase signalling networks in cancer. *Frontiers in Cell and Developmental Biology.* **8**, 222. (doi: 10.3389/fcell.2020.00222).

[86] Haga RB, Ridley AJ. 2016. Rho GTPases: regulation and roles in cancer cell biology. *Small GTPases.* **7**, 207–221. (doi: 10.1080/21541248.2016.1232583).

[87] Sabass B, Gardel ML, Waterman CM, Schwarz US. 2008. High resolution traction force microscopy based on experimental and computational advances. *Biophysical Journal.* **94**, 207–220. (doi: 10.1529/biophysj.107.113670).

[88] Pertz O, Hahn KM. 2004. Designing biosensors for Rho family proteins–deciphering the dynamics of Rho family GTPase activation in living cells. *Journal of Cell Science.* **117**, 1313–1318. (doi: 10.1242/jcs.01117).

[89] Houk A, Jilkine A, Mejean C, Boltyanskiy R, Dufresne E, Angenent S, Altschuler S, Wu F, Weiner O. 2012. Membrane tension maintains cell polarity by confining signals to the leading edge during neutrophil migration. *Cell.* **148**, 175–188. (doi: 10.1016/j.cell.2011.10.050).

[90] Sharma S, Santiskulvong C, Rao J, Gimzewski JK, Dorigo O. 2014. The role of Rho GTPase in cell stiffness and cisplatin resistance in ovarian cancer cells. *Integrative Biology*. **6**, 611–617. (doi: 10.1039/c3ib40246k).

[91] Wentz JM, Mendenhall AR, Bortz DM. Pattern formation in the longevity–related expression of heat shock protein-16.2 in Caenorhabditis elegans. *Bulletin of Mathematical Biology*. **80**, 2669–2697. (doi: 10.1007/s11538-018-0482-7).

[92] Turing A. 1952. The chemical basis of morphogenesis. *Philosophical Transactions of the Royal Society B: Biological Sciences*. **237**, 37–72. (doi: 10.1098/rstb.1952.0012).

[93] Codling EA, Plank MJ, Benhamou S. 2008. Random walk models in biology. *Journal of the Royal Society Interface*. **5**, 813–834. (doi: 10.1098/rsif.2008.0014).

[94] El-Hachem M, McCue SW, Simpson MJ. 2020. A sharp–front moving boundary model for malignant invasion. *Physica D: Nonlinear Phenomena*. **412**, 132639. (doi: 10.1016/j.physd.2020.132639).

[95] Provenzano PP, Keely PJ. 2011. Mechanical signalling through the cytoskeleton regulates cell proliferation by coordinated focal adhesion and Rho GTPase signalling. *Journal of Cell Science*. **124**, 1195–1205. (doi: 10.1242/jcs.067009).

[96] Wang H, Anderson M. 1982. *Introduction to Groundwater Modeling Finite Difference and Finite Element Methods*. San Diego: Academic Press.

[97] Kelley C. 2003. *Solving Nonlinear Equations with Newton's Method*. Philadelphia: Society for Industrial and Applied Mathematics.

[98] MathWorks `quiver`. Retrieved from https://au.mathworks.com/help/matlab/ref/quiver.html in July 2020.

[99] Wyatt T, Baum B, Charras G. 2016. A question of time: tissue adaptation to mechanical forces. *Current Opinion in Cell Biology*. **38**, 68–73. (doi: 10.1016/j.ceb.2016.02.012).

[100] Anguige K, Schmeiser C. 2009. A one–dimensional model of cell diffusion and aggregation, incorporating volume filling and cell-to-cell adhesion. *Journal of Mathematical Biology*. **58**, 395. (doi: 10.1007/s00285-008-0197-8).

[101] Hanahan D, Weinberg RA. 2011. Hallmarks of cancer: the next generation. *Cell.* **144**, 646–674. (doi: 10.1016/j.cell.2011.02.013).

[102] Martin P. 1997. Wound healing–aiming for perfect skin regeneration. *Science.* **276**, 75–81. (doi: 10.1126/science.276.5309.75).